Reconstructing Pyroclastic Currents' Source and Flow Parameters from Deposit Characteristics and Numerical Modelling: The Pozzolane Rosse Ignimbrite case study (Colli Albani, Italy)

Laura Calabrò[1*], Tomaso Esposti Ongaro[2], Guido Giordano[1,3], Mattia de' Michieli Vitturi[2,4]

[1] Dipartimento di Scienze – Sezione Geologia, Università di Roma Tre, Roma, Italy.
[2] Istituto Nazionale di Geofisica e Vulcanologia, Sezione di Pisa, Pisa, Italy.
[3] Istituto di Geologia Ambientale e Geoingegneria, CNR, 00010 Montelibretti, Italy.
[4] Department of Geology, University at Buffalo, 126 Cooke Hall, Buffalo, New York 14260, USA.

*Corresponding author: Laura Calabrò (laura.calabro@uniroma3.it)

Key Points:

- A new depth-averaged, equilibrium mixture model for pyroclastic currents is used to study the main features of caldera-forming ignimbrites.
- The ignimbrite runout and thickness decay pattern are correlated to three main flow source parameters.
- The main properties of the flow that generated the Pozzolane Rosse ignimbrite are reconstructed.

Abstract

In this study, we apply a two-dimensional, transient depth-averaged model to simulate the inertial flow dynamics of caldera-forming pyroclastic currents, using the available data about the Pozzolane Rosse ignimbrite (Colli Albani, Italy) eruption (460 ka, 63 km^3 DRE). By performing an extensive set of numerical simulations, we test the effects of the initial parameters of the pyroclastic current (Richardson number, mass flow rate, initial flow density) on simulated deposit characteristics which can be compared with selected ignimbrite field observables, including the deposit dispersal along topography, the maximum distance from source, the deposit thickness, the grain size distribution at different distances, and the emplacement temperature. Results permit us to quantify the first-order dependency of the flow runout on the mass flow rate, and of the deposit thickness decay pattern on the initial mixture density. By using the results of the parametric study we reconstruct the source parameters of the Pozzolane Rosse ignimbrite constrained by the ignimbrite depositional characteristics, including the mass partition into the co-ignimbrite cloud. Despite uncertainties associated with the complex, non-linear interplay between the flow variables, the single-layer, depth-averaged model demonstrates to be suitable for simulating inertial pyroclastic currents, such as those generating large-scale caldera-forming ignimbrites, providing a tool for reconstructing the eruption source parameters from deposits characteristics, and to assess pyroclastic currents' hazard for future eruptions.

Plain Language Summary

Pyroclastic currents are hot mixtures of gas and pyroclastic particles generated during explosive eruptions, which travel along topography at moderate to very high speed (tens to hundreds of m/s) under the effect of gravity. Pyroclastic currents, generated during large volcanic eruptions (often associated with formation of calderas), can travel tens of km far from the eruptive center and are able to pass topographic obstacles up to hundreds of metres high. These characteristics make them one of the most dangerous and inaccessible natural phenomena to study. For these reasons, the use of numerical modelling is essential to provide key quantitative information about pyroclastic currents' internal dynamics. In this study, we apply a new numerical simulation model to reconstruct the eruption conditions generating the Pozzolane Rosse ignimbrite (Colli Albani, Italy, 460 thousand years ago). Simulation results permit us to explain the dependency of the observable field data (flow runout, deposit thickness, grain-size and temperature) on the initial flow conditions (thickness, velocity, density, temperature and grain-size distribution).

Despite the uncertainties still affecting the methodology we are able to invert field characteristics of the Pozzolane Rosse ignimbrite to constrain the initial mass flow rate and density of the parent pyroclastic current.

1 Introduction

Pyroclastic Currents (PCs; Palladino, 2017) are the most hazardous phenomena produced by volcanic eruptions. PCs are hot mixtures of gas and pyroclastic particles, which travel at moderate to very high speed (tens to hundreds of m/s) under the effect of their density difference with the surrounding atmosphere (Cas and Wright, 1987; Druitt, 1998; Branney and Kokelaar, 2002; Sulpizio et al., 2014; Dufek, 2016).

Due to their inherently destructive and dangerous nature, direct *in-situ* measurements of flow parameters (e.g., particle concentration, velocity, temperature) are still not possible, while remote sensing techniques are in progress (Bignami et al., 2013; Scharff et al., 2019; Calvari et al., 2020). For these reasons, studies on PCs deposits (Wilson and Walker, 1982; Wilson et al., 1995; Giordano, 1998; Wilson, 2001; Sulpizio et al., 2007; Cas et al., 2011; Giordano and Cas, 2021) and their modeling, both analogue (Lube et al., 2015; Roche, 2012, 2015; Gueugneau et al., 2017; Breard et al., 2017, Dellino et al., 2007, 2019; Weit et al., 2019) and numerical (Valentine et., 2011; Dufek, 2016; Esposti Ongaro et al., 2011, 2012, 2016, 2020; Valentine and Sweeney, 2018) provide the most valuable insights into the transport and depositional mechanisms.

Conventionally, PCs deposits are distinguished on the basis of their lithofacies. The wide variety of PCs deposits suggests that there is a continuous spectrum of flow types between end-members (Branney and Kokelaar, 2002; Sulpizio et al., 2014, Giordano and Doronzo, 2017). The classical and most intuitive dichotomy distinguishes between dilute and concentrated regimes of PCs (Cas and Wright, 1987; Giordano, 1998; Wohletz, 1998; Branney and Kokelaar, 2002; Burgisser and Bergantz, 2002; Sulpizio et al., 2014; Brown and Andrews, 2015; Palladino, 2017; Roche et al., 2021).

The dilute regime is characterized by particle concentration below a few volume percent (i.e. flow density < ~10 kg/m^3), where the particle support is dominated by the turbulence of the gas phase. In the dilute regime, energy dissipation due to viscosity of the gas phase and particle-particle collisions are negligible (Dade and Huppert, 1996; Dufek et al., 2016; Esposti Ongaro et al., 2016), and the dynamics are inertial. The loss of PCs momentum is mainly controlled by the rate of particle sedimentation and by the rate of air entrainment, which eventually lead to positive buoyancy and current lift-off. Turbulence significantly contributes to momentum diffusion, but its main role is that of controlling air entrainment, which causes a significant increase in flow volume. Dilute inertial PCs are typified by expanded (hundreds of metres thick) base-surges, which can travel across high reliefs (of the order of their thickness) with internal turbulence able to maintain suspended most of the transported pyroclasts (Andrews, 2014). The rates of air entrainment are high and cause the significant increase in the flow volume. The basal layer (formed by the sedimentation of the solid particles) is thin with respect to the overall thickness of the laterally moving dilute PCs and it is unable to move independently, leaving relatively cold and (cross-)stratified deposits.

At the other end-member, the concentrated regime is characterized by high particle concentrations, in the order of tens of vol% (i.e. flow density 100-1000 kg/m^3), where particle transport is dominated by particle-particle interactions (collisions and frictional contacts) and/or interstitial fluid escape (pore pressure; Roche et al., 2011, 2021; Lube et al., 2020). In the concentrated regime, the dynamics are mostly controlled by granular friction, which dissipates momentum and energy, counter-acted by pore pressure, which alleviates particle interactions. Concentrated frictional PCs are typified by block-and-ash flows generated by dome collapse, in which most of the PCs mass travels confined within volcano valleys and is controlled by its relatively thick, high concentration basal zone. The basal concentrated flow is able to move until condition for onset of deposition are reached, leaving massive, hot, thick and valley-pond deposits (Ui et al., 1999; Cole et al., 2002; Lube et al., 2007; Pensa et al., 2018).

Both dilute and concentrated regime coexist in most real PCs due to the internal stratification of concentration and velocity (Druitt, 1998; Giordano, 1998; Branney and Kokelaar, 2002; Roche et al., 2013; Pensa et al., 2019). Such intermediate regimes are the most difficult to describe, owing to the complex gas-particleand particle-particle interactions and particle clustering processes, which are still matter of fundamental research (Weit et al., 2018; 2019; Lube et al., 2020).

Among the most enigmatic (and historically debated) flow types are large-scale PCs associated with caldera-forming eruptions (Giordano and Cas, 2021), which usually leave massive, valley pond and thick ignimbrite deposits (e.g. Cerro Galan; Cas et al., 2011; Peach Spring Tuff; Roche et al., 2016), but can also pass high reliefs leaving or not veneer deposits (e.g. Taupo ignimbrite, Wilson and Walker, 1982; Campanian ignimbrite; Fisher et al., 1993, Silleni et al., 2020; Ito ignimbrite, Baer et al., 1997). In most known large caldera-forming ignimbrites (Giordano and Cas, 2021), the common radial distribution across highly variable topographies (from flat to mountain areas) suggests that the basal high concentration layer comes to an halt rather quickly while the lateral transport is guaranteed by the over-riding dilute layer (e.g. Shimizu et al., 2019). For these reasons, in this study, we hypothesize, in agreement with previous studies by Bursik and Woods (1996) and Dade and Huppert (1995), that the transport system of some large caldera-forming PCs, while not necessarily dilute in a strict sense, can be described as inertial flows, controlled by particle sedimentation and air entrainment. In these kinds of PCs the processes occurring in the basal concentrated layer control the sedimentary facies of the resulting ignimbrite (e.g. massive vs stratified), but do not significantly affect the large-scale transport dynamics associated with the over-riding dilute and turbulent flow.

The understanding of large-scale PCs dynamics is still largely debated around depositional facies of the resulting ignimbrites, so the definition of methods to link measurable deposit characteristics and eruptive and flow parameters (including mass flow rate, flow velocity, flow thickness, concentration and temperature) is of paramount importance although not yet achieved. Numerical modelling represents an essential tool to investigate such links, provided that appropriate measured deposit characteristics are available and that dedicated numerical codes are developed.

Recent works by Roche et al. (2021) and Giordano and Cas (2021) have explored a number of first order field descriptors for a relatively large number of ignimbrites, which can be correlated with eruption and flow dynamics. Roche et al. (2021) used statistical methods to quantify the control of mass discharge rate on the runout distance of PCs. Giordano and Cas (2021) proposed a classification scheme for ignimbrites and their eruptions emphasizing the increasing power law relationship between runout and volume, which are proxies respectively for eruption intensity (mass discharge rate) and magnitude (mass), with the aspect ratio (the ratio of the average thickness of the deposit to the horizontal extent and/or the thickness decay patterns) defining the attitude to topography, varying from filling, to draping to burying. Based on the above, we select the following ignimbrite field descriptors to constrain numerical PC simulations:

(i) the maximum distance at which deposits are found, as a proxy for the maximum distance reached by the flow (i.e. runout);

(ii) the total erupted volume (see Mason et al., 2004 and Silleni et al., 2020 for a discussion on the sources of error and uncertainties);

(iii) the deposit geometry, i.e. areal distribution, aspect ratio (Wilson, 1991; Giordano and Doronzo, 2017; Silleni et al., 2020);

(iv) the temperature of emplacement (e.g. Lesti al., 2011; Pensa et al., 2015, 2019; Trolese et al., 2017, 2018);

(v) the total grain size distribution, a parameter rarely estimated for ignimbrites and which inherently underestimates the finest fraction elutriated into the co-ignimbrite ash cloud.

(vi) the type of interaction with the topography (e.g., the maximum height overpassed; Giordano and Dobran, 1994),

In this work, we use all of the above field characteristics available for the caldera forming, 460 ka, 63 km^3 DRE, Pozzolane Rosse ignimbrite (Colli Albani, Italy; Giordano and Dobran, 1994; Giordano et al., 2010) to model source and flow dynamics with a transient, depth-averaged model for inertial PCs over a rough topography, accounting for the sedimentation from a polydisperse gas-pyroclasts mixture and turbulent air entrainment. Results are relevant in general for PCs associated with caldera-forming ignimbrites, whose transport system can be described as inertial, opening a new horizon for PC numerical experiments which link ignimbrite characteristics to flow source and transport parameters.

2 Depth-averaged approach to PC modelling

Sparks and Wilson (1976) and Sparks et al. (1978) were the first to describe the dynamics of pyroclastic flows by considering a homogeneous dispersion of gas and pyroclasts, by using a set of equations obtained from a depth-averaging of the Neavier-Stokes equation. By vertically averaging the flow fields (velocity, particle concentration, temperature), such modeling strategy cannot account for the effects of the internal vertical stratification captured by multidimensional models (e.g., Giordano and Dobran, 1994; Neri et al., 2003; Dufek and Bergantz, 2007; Esposti Ongaro et al., 2012), but PC flow fields can be described in their radial distribution, from the source to the final runout. A depth-averaged modelling strategy, describing the axisymmetric spread of gravity currents, was developed by Bursik and Woods (1996) (hereineafter referred to as BW96), who integrated the energy equation and the thermodynamics of gas-particle mixtures, and demonstrated that the dynamics of large-scale PCs are largely controlled by atmospheric air entrainment (which increases the current gas fraction and volume) and particle sedimentation (which subtracts mass and momentum to the bulk flow). Both processes contribute to the decrease in PCs bulk density that eventually leads to buoyancy reversal. In addition, BW96 suggested that pyroclastic current dynamics are controlled by a non-dimensional parameter, called the Richardson number, corresponding to the inverse of the squared Froude number (i.e. $\mathrm{Ri} = \frac{1}{\mathrm{Fr}^2}$; Dade and Huppert, 1995b). The Richardson number is defined as:

$$\mathrm{Ri} = \frac{(\rho_m - \rho_a)gh}{\rho_m v^2} = \frac{g'h}{v^2} \qquad \text{eq. 1}$$

where ρ_m is the flow density, ρ_a is the atmospheric air density, g is the gravitational acceleration, h is the flow thickness, v is flow velocity and g' is reduced gravity. Two different regimes for inertial currents were thus identified by BW96: subcritical ($\mathrm{Ri} > 1$) and supercritical flows ($\mathrm{Ri} < 1$).

Depth-averaged isothermal models have also been used to describe high concentration PCs (Patra et al., 2005; Kelfoun and Druit, 2005; de' Michieli Vitturi et al., 2019). In these models, friction is usually described by the Coulomb rheology (Savage and Hutter, 1989), but the debate about the optimal rheological model is still ongoing (Kelfoun et al., 2009, Gueugneau et al., 2017). To approach more realistically the vertical stratification of PCs depth-averaged models have been integrated in two-layers models for the dilute upper current and concentrated basal layer (Doyle et al., 2010; Kelfoun, 2017; Shimizu et al., 2019). In particular, Shimizu et al. (2019) integrated the transient BW96 model for the upper dilute layer with a depth-averaged model for the basal, frictional flow. Their results demonstrate that the flow runout critically depends on the relative rates of mass transfer between the upper dilute and the lower concentrated layers, and from the lower concentrated layer to the deposit, both of which need more theoretical and experimental studies to be appropriately calibrated.

2.1 Simulation approach and assumptions

In this study, in agreement with BW96, we adopt a one-layer, depth-averaged model to study the dynamics of inertial PCs related to intermediate to large-volume caldera-forming ignimbrites (>VEI 6; Giordano and Cas, 2021). This approach is considered suitable for flows where most of the mass is transported in the dilute part and wherein the dynamics of the basal concentrated underflow does not significantly affect the dynamics of the overlying flow, and can therefore be, at first order, disregarded.

Our model extends the BW96 approach by considering transient flows over a three-dimensional rugged surface (representing the topography), and a polydisperse mixture. The model neglects the effect that the basal concentrated layer might have on the propagation of PCs (Roche et al., 2016; Esposti Ongaro et al., 2016), assuming that the deposition is near-instantaneous. Such an assumption is valid in absence of a significant topographic slope, which may accelerate the basal concentrated layer thus favouring flow decoupling (e.g. Fisher, 1995); and when most of the erupted mass is kept in suspension along the flow runout (due to a combination of large flow thickness and low particle settling velocity).

3 Case Study: The Pozzolane Rosse Ignimbrite

The Pozzolane Rosse ignimbrite is the largest of the caldera-forming eruptions of the Colli Albani volcano (Giordano et al., 2006, 2010). The ignimbrite originated from a mafic (tephritic in composition; Boari et al., 2009; Conticelli et al., 2010) and low-viscosity magma (Campagnola et al., 2013), dated at 457±4 ka (Freda et al., 2011). The origin of the explosivity of such mafic and low-viscosity magma is still poorly understood, generally attributed either to the role of crustal thermometamorphic CO_2 (Freda et al., 2011), or to mantle-derived CO_2 gas sparging on a water saturated shallow magma chamber (Vinkler et al., 2012), both consistent with the high deep CO_2 flux in the region (Chiodini and Frondini, 2001; Tuccimei et al., 2006). It is a low aspect ratio ignimbrite (mean thickness/ mean length = 4×10^{-4} ;Giordano and Cas, 2021) with an estimated total DRE volume of 63 km^3 (Giordano et al., 2010) and a maximum distance from the central vent measured at 33 km (Giordano and Dobran, 1994; Giordano and Doronzo, 2017). Deposits are distributed symmetrically around the 8 km–radius central caldera (Fig. 1a), largely on a flat topography, but also across a high relief located to the east of the caldera. There, the ignimbrite is found across more than 440 m high topographies and valley confined, although its maximum distance from source is the same as in flat areas, depicting an axisymmetric distribution (Giordano and Doronzo, 2017; Smith et al., 2020). The RED eruption rate was estimated at 10^9 kg/s (Giordano and Dobran, 1994; BW96). The temperature of emplacement for the RED ignimbrite was estimated by paleomagnetism higher than 630°C across its entire extent although the ignimbrite is nowhere welded, indicating a maximum drop in temperature of 100°C/km (Trolese et al., 2017). At the base of the ignimbrite a reverse-graded scoria lapilli fallout deposit is present (Fig.1b), with a maximum thickness of 70 cm and an ENE-trending dispersal axis (Giordano et al., 2010; Freda et al., 2011). The main RED ignimbrite is massive, coarse-ash matrix supported lapilli tuff (Fig. 1b, c, d). This facies consists of reddish-purple to dark grey, poorly to moderately vesicular, scoria lapilli (up to 30 cm in diameter) and lithic clasts (up to 8 cm in diameter) in a crystal and coarse-ash shard matrix (60 – 90%; Giordano et al., 2010). It characteristically contains thermally metamorphosed sedimentary accessory lithic clasts. The ignimbrite is generally unconsolidated and, in some places, moderately lithified due to vapor-phase zeolite crystallization. Gas-pipes and columnar jointing are observed especially where confined in paleovalleys. The ignimbrite forms a tabular sheet that can be up to 80 m thick (at a break in slope of the volcano, in paleovalleys and in front of the Apennine Mountains), with an average thickness ranging from 10 to 30 m (Fig. 1a; Giordano and Dobran, 1994).

The fairly monotonous lithofacies of the deposit both vertically and downcurrent, as far as the most distal reaches, underlines steady conditions for sedimentation. Only close to substantial topographical reliefs, the ignimbrite is internally crudely stratified (Giordano and Doronzo, 2017; Smith et al., 2020). The ignimbrite is in general poor in fine ash (less than 15 wt%). At increasing distance from vent, there is a significant shift of the grain size curves towards the finer grained classes, with a mean size that varies from +1 to -1Φ (Rosa, 1987; Supplementary Information SM1), as well as of lithic and scoria lapilli sizes. At ~100 km east from the source, a 7 cm-thick deposit made of well-sorted, coarse ash to fine lapilli has been interpreted as coignimbritic in origin (Giaccio et al., 2013).

4 The numerical model

4.1 Depth-averaged equations

The model describes the propagation of an incompressible turbulent gravity current, as a homogeneous mixture of gas (atmospheric air) and n solid particles in thermal and kinetic equilibrium with the gas. The local, average density of the current, ρ_m, is given by:

$$\rho_m = \left(1 - \sum_{i=1}^{n} \varepsilon_{\mathrm{i}}\right)\rho_g(T) + \sum_{i=1}^{n} \rho_i \varepsilon_{\mathrm{i}} \qquad \text{(eq. 2)}$$

where ρ_g is the gas density (depending on the mixture temperature T through the perfect gas equation of state), ε_{i} is volume fraction of the i^{th} particle class, and ρ_i is the particle density.

The model solves the depth-averaged equations for conservation of mass, momentum, and energy of the mixture, and one mass transport equation for each solid phase including the effects of air entrainment, particle deposition and friction. Vertical accelerations are neglected in the process of depth-averaging, so the pressure is hydrostatic. Finally, the volcano topography is accounted for by integrating a Digital Elevation Model as a function $B(x, y)$.

The equations of conservation of mass (eq.3), momentum (eq.4) and energy (eq.5) for the mixture, and of mass for the solid phases are written in a system of geographical Cartesian UTM coordinates (x, y):

$$\frac{\partial(\rho_m h)}{\partial t}+\frac{\partial(\rho_m v_x h)}{\partial x}+\frac{\partial(\rho_m v_y h)}{\partial y}=\sum_{i=1}^{n_p}\left[-\rho_i D_{p_i}\right]+\rho_a \mathrm{E_a} \qquad \text{eq. 3}$$

$$\frac{\partial(\rho_m v_x h)}{\partial t}+\frac{\partial}{\partial x}\left(\rho_m v_x^2 h+\frac{1}{2}\rho_m g' h^2\right)+\frac{\partial}{\partial y}\left(\rho_m v_x v_y h\right)$$

$$=\rho_m g' h\frac{\partial B}{\partial x}+F_x-v_x\sum_{i=1}^{n_p}\left[-\rho_i D_{p_i}\right] \qquad \text{eq. 4a}$$

$$\frac{\partial(\rho_m v_y h)}{\partial t}+\frac{\partial}{\partial x}\left(\rho_m v_x v_y h\right)+\frac{\partial}{\partial y}\left(\rho_m v_y^2 h+\frac{1}{2}\rho_m g' h^2\right)$$

$$=\rho_m g' h\frac{\partial B}{\partial y}+F_y-v_y\sum_{i=1}^{n_p}\left[-\rho_i D_{p_i}\right] \qquad \text{eq. 4b}$$

where h is the flow thickness; v_x and v_y are the horizontal components of the flow velocity; D_p represents the volumetric deposition rate of solid particles rate from the dilute flow to the concentrated basal layer; $\mathrm{E_a}$ is the volumetric air entrainment rate; F_x and F_y are the friction terms along the x and y directions; g' is the reduced gravity ($g' = [(\rho_m - \rho_a)/\rho_m]g$). Both air entrainment and particle sedimentation are crucial for modelling changes in flow density with respect to distance from source. Moreover, the mixture temperature (T) changes with entrainment of air. Therefore, for the conservation of mixture specific energy ($e = C_v T + \frac{1}{2}(v_x^2 + v_y^2)$) the following equation is written:

$$\frac{\partial}{\partial t}(\rho_m h e) + \frac{\partial}{\partial x}\left[\left(e + \frac{1}{2}g'h\right)\rho_m h v_x\right] + \frac{\partial}{\partial y}\left[\left(e + \frac{1}{2}g'h\right)\rho_m h v_y\right] = -\rho_m g' h\left(v_x\frac{\partial B}{\partial x} + v_y\frac{\partial B}{\partial y}\right) - \frac{1}{2}\left(v_x^2+v_y^2\right)\sum_{i=1}^{n_p}\left(\rho_i D_{p_i}\right) - \sum_{i=1}^{n_p}\left(\rho_i C_p T D_{p_i}\right) + C_a\rho_a T_a \mathrm{E_a} \qquad \text{eq. 5}$$

where C_v is the mass averaged specific heat in the flow, C_p and C_a are the specific heats of solid particle and air, respectively, and T_a and T are the temperature of the atmosphere and of the PC mixture respectively.

Additionally, conservation equation for the mass of solid classes are also considered:

$$\frac{\partial(\varepsilon_i\rho_i h)}{\partial t} + \frac{\partial(\varepsilon_i\rho_i v_x h)}{\partial x} + \frac{\partial(\varepsilon_i\rho_i v_y h)}{\partial y} = -\rho_i(D_{p_i}) \qquad \text{eq. 6}$$

4.2 Air Entrainment

The entrainment of air plays an important role in gravity current propagation. In stratified flows, the entrainment depends on the ratio of the potential energy of a parcel of the overlying buoyant fluid, which has to be entrained in the current, and the mean kinetic energy of the flow (Turner, 1986; Bursik and Woods 1996). This ratio is expressed by the Richardson number (see eq. 1). Usually, Ri < 1 implies the predominance of inertial effects (greater instability) and a higher entrainment rate in the upper part of the flow; the air entrainment rate is expected to be a decreasing function of the Richardson number. Following BW96, we adopt the Turner (1986) formulation, based on the experiments made by Ellison and Turner (1959). Accordingly, the air entrainment rate in eqs. (3) and (5) is written as a function of the Richardson number, in which

$$E_a = \epsilon\sqrt{(v_x^2 + v_y^2)} \qquad \text{eq. 7}$$

where ϵ is the entrainment coefficient given by

$$\epsilon = \frac{0.075}{(1 + 718\mathrm{Ri}^{2.4})^{0.5}} \qquad \text{eq. 8}$$

4.3 Sedimentation

Sedimentation of particles (D_p) is assumed proportional to the settling velocity (v_s) as for dilute flows and, in our model, once the particles are incorporated in the basal concentrated layer (i.e.

once particles settle below the base of our computational domain; Fig. 2), they cannot be re-incorporated by the flow (Fauria et al., 2016):

$$D_{p_i} = \varepsilon_i \, v_s(d_i) \left(1 - \frac{\sum \varepsilon_i}{\varepsilon_{i-max}}\right)^n \qquad n > 1 \qquad \text{eq. 9}$$

The factor $\left(1 - \frac{\sum \varepsilon_i}{\varepsilon_{i-max}}\right)^n$ accounts for reduced sedimentation by hindered settling, in which ε_{i-max} is the maximum volume fraction (usually is considered between 0.6 and 0.7), d_i is diameter of the particle; n is an empirical exponent (4.65 is considered for solid spheres; Bürger and Wendland, 2001). The settling velocity, v_s, is obtained by the following equation:

$$\frac{4}{3} d_i g \frac{(\rho_i - \rho_a)}{\rho_a} = C_D(Re) v_s^2(d_i) \qquad \text{eq. 10}$$

where C_D is a drag factor given by

$$\text{if} \begin{cases} \text{Re} < 1000; & C_D = \frac{24}{\text{Re}}(1 + 0.15 \times \text{Re}^{0.685}) \\ \text{Re} > 1000; & C_D = 0.44 \end{cases} \qquad \text{eq. 11}$$

where Re is the Reynolds number:

$$\text{Re} = \frac{d_i v_s}{\mu} \qquad \text{eq. 12}$$

μ is the kinematic viscosity of the carrier fluid (air, for dilute PCs). Solving for the settling velocity $v_s(d_p)$, we obtain:

$$v_s(d_i) = \sqrt{\frac{4(\rho_i - \rho_a)}{3\rho_a C_D} d_i g} \qquad \text{eq. 13}$$

This equation cannot be resolved explicitly since C_D depends on v_s. Therefore, an iterative procedure is implemented to solve for the settling velocity.

4.4 Input parameters and simulated scenarios

In our application, we assume that the PC feeding is sustained for a time longer than that needed for the front to reach the maximum runout. We also assume a steady feeding during the whole duration of the simulation (imposing an unsteady feeding would anyway be possible with the model). In the following, for the flow variables at the inlet, we will use the superscript 0.

Boundary conditions represent the radial injection of the multiphase flow mixture from a cylindrical surface of radius R^0 and height h^0 (Fig. 2). The value of R^0 should be large enough in order to disregard the effects of the complexity of source conditions on the PC propagation. In our study a value of R^0=3 km has been used (Supplementary Information SM3), which approximates the caldera radius and can be consistent with an eruption fed by ring fractures (Roche et al., 2000; Geyer et al., 2004; Giordano and Cas, 2021).

We assume that the flow is initially in supercritical regime (Bursik and Woods, 1996; Shimizu et al., 2019), i.e. its velocity is larger than the surface wave velocity. For supercritical flows, the values of h^0, v^0, ρ^0, T^0 and ε^0 are input parameters to be assigned at the inlet boundary. We also assume that the initial velocity does not exceed the speed of sound in the air (v^0 < 340 m/s; Dade and Huppert, 1996; Dade, 2003). Above the speed of sound, the compressibility effects start to be dominant and would not be properly modelled by our model. It should be noted that the speed of sound in particle dispersions is lower than in air (340 m/s), potentially down to 100 m/s (Kieffer and Sturtevant, 1984; Esposti Ongaro et al., 2011). This assumption on the initial velocity is supported by experimental results (Dade and Huppert 1995a, 1995b; Dade et al., 1994) on turbulent gravity currents radially spreading from a source with constant volume. Observation and theoretical considerations (Benjamin, 1968) suggest indeed that the flow Froude number (Fr, i.e. the ratio between the front velocity and the wave velocity) should be around $\sqrt{2}$; (Ellison and Turner, 1959; Benjamin, 1968; Huppert and Simpson, 1980). Because the Richardson number Ri is equal to $\frac{1}{(\mathrm{Fr})^2}$, we investigate regimes with initial condition $Ri^0 = 0.5$ (nearly critical), but also explore $Ri^0 = 0.05$ (supercritical). We also restrict our investigation to a range of average mixture densities between ~1 (atmospheric density) and ~100 kg/m^3 (Dade, 2003). This is consistent with various estimates of flow density at column collapse from numerical modelling (e.g., Esposti Ongaro et al., 2008b; Trolese et al., 2019). Moreover, we consider that above a mixture density of 100 kg/m^3, the (average) total particle concentration would be > ~0.05, a threshold above which particle-particle collisions and frictional forces are thought to be dominant in flow propagation dynamics (Dufek, 2016; Lube et al., 2020) and clusters are likely to form (Lube et al., 2020). A set of values of 9.70 kg/m^3, 23.65 kg/m^3 and 70.14 kg/m^3 was selected.

To enforce these constraints, we express the inflow boundary conditions on $(h^0,\ v^0,\ \rho_m^0)$ in terms of $(\dot{m}^0,\ Ri^0,\ \rho_m^0)$, through of the following transformations:

$$\begin{cases} \dot{m}^0 = 2\pi r v h^0 \rho_m^0 \\ Ri^0 = \dfrac{(\rho_m^0 - \rho_a) g h^0}{\rho_m^0 v^2} \end{cases} \rightarrow \begin{cases} h^0 = \dfrac{\dot{m}^0}{(2\pi v \rho_m^0)} \\ v = \sqrt[3]{\dfrac{\dot{m}^0\ (\rho_m^0 - \rho_a)g}{2\pi r (\rho_m^0)^2\ Ri^0}} \end{cases} \qquad \text{eq. 14}$$

We then explored, by means of numerical simulations, the dynamics of PCs and their associated deposits in the range of inputs reported in Table 1. It is worth noting that at low-Ri, lower density flows need velocities above the speed of sound to maintain higher mass flow rates. Therefore, we hypothesize that supercritical flows more likely occur with higher density values. In the parametric analysis (Table 1 and 2), we assumed an initial total volume particle concentration (ε^0) of 0.015, 0.005 and 0.002 with three grain sizes (200 μm, 1 mm, 1.6cm; Giordano and Dobran, 1994) having equal concentration. The inlet flow temperature (T^0) has been selected between 873 and 973 K (cf. Trolese et al., 2017).

4.5 Computational domain and simulation conditions

We assume a homogeneous current with a constant inlet mass flow rate for a time of 500 seconds first on a flat surface and then on the topography of Colli Albani. The computational domain is 80×80 km and is discretized by a regular grid with 800×800 cells (cell size of 100 m). A preliminary study has been performed on the effects of the grid size to ensure that the resolution is adequate to simulate the PCs (see Supplementary material SM3). The centre of the cylinder is located at the UTM coordinates [813050, 4629000]. Because the source conditions are axisymmetrical, in absence of topography, the results should be invariant along the azimuthal directions (we will therefore present only radial trends). We observe that the inlet velocity should be prescribed at the lateral surface of the inlet cylinder, but the faces of the computational cells where the boundary conditions are prescribed do not lie exactly on it. For this reason, a correction on the velocity accounting for this discrepancy is applied on each inlet face. We verified that, even if we use a cartesian grid, the second-order discretization in space implemented in the model, coupled with the correction on the velocity components prescribed at the inlet faces, produce axisymmetric flows.

5 Results of the parametric study

We initially adopted a flat topography to perform a parametric study, identifying the first-order control of input flow parameters onto the selected observables: runout, deposit shape and thickness. These results permit us to highlight the dependence of the output parameters on the input parameters and to identify the most suitable initial condition to simulate the RED case study.

5.1 Influence of initial mass flow rate (at fixed ρ_m^0 and Ri^0)

This section presents the results of the numerical simulations at the last time step (500 s), when the PCs have reached the steady-state regime. These simulations were performed to examine the effect of mass flow rate on PCs runout. Here, we report only the flows with $\dot{m}^0$ between 10^9 and 10^{10} kg/s, ε^0=0.005 and T^0 =873 K. Table 1 summarizes the input conditions of the simulations. As discussed above, the model produces a radial distribution of flow variables $(h, v, \rho, \varepsilon_i, T)$. In addition, it provides the deposit radial distribution for all particle classes and an integral measure of the mass flow rate (for each particle class) that feeds the co-ignimbrite plume when the radial flow stops and lifts-off. We remark that the simulations described here are 2D simulations with a radial source and a flat topography, and for this reason they result in an axisymmetric flow with a radial distribution of variables.

Fig. 3 illustrates the trend of the flow velocity, thickness, density, and temperature versus the distance from source for $Ri^0 = 0.5$ and $Ri^0 = 0.05$.In these graphs, a clear difference is observed in the flow dynamics between the two values of Ri^0. In flows with $Ri^0 = 0.5$, the velocity (Fig. 3a) increases up to 3-5 km distance, where it reaches its maximum values, ranging from 69 to 165 m/s, at increasing $\dot{m}^0$. Then, the velocity decreases to values ranging from 47 to 84 m/s. Flow thickness decreases within the first 2 km, before turning to a steady increase (Fig. 3b). Maximum flow thickness ranges from 370 m to 1069 m, at increasing $\dot{m}^0$. The flows reach maximum distances ranging from 11.7 km ($\dot{m}^0$ = 6.36×10^9 kg/s) to 37.3 km ($\dot{m}^0$ = 6.82×10^{10} kg/s).

For flows with $Ri^0 = 0.05$, for which the initial flow velocity is much higher than with $Ri^0 = 0.5$, flow velocity steadily decreases with the distance (Fig. 3e). The final velocity at lift-off displays higher values compared to simulations with Ri^0 = 0.5, ranging from 69 m/s ($\dot{m}^0$ = 6.36×10^9 kg/s) to 146 m/s ($\dot{m}^0$ = 6.82×10^{10} kg/s). The flow thickness (Fig. 3f) increases steadily over distance, due to the enhanced air entrainment and it reaches maximum values spanning from 548 to 1843 m at increasing $\dot{m}^0$. The maximum distances reached by the flow after 500 s range from 11.4 km ($\dot{m}^0$ = 6.36×10^9 kg/s) to 29.5 km ($\dot{m}^0$ = 6.82×10^{10} kg/s), lower than for flows with $Ri^0 = 0.5$.

Concerning flows densities (Fig. 3c and 3g) and temperatures (Fig. 3d and 3h), the graphs show that flows with higher entrainment ($Ri^0 = 0.05$) have density and temperature that decrease rapidly with distance from source.

5.2 Influence of the initial mixture density (at fixed $\dot{m}^0$ and Ri^0)

This section presents the results of numerical simulations carried out varying the initial mixture density ρ_m^0 at same $\dot{m}^0$(6.82×10^{10} kg/s). These simulations were performed at $Ri^0 = 0.5$ and $Ri^0 = 0.05$ to examine the effects of the initial mixture density on the radial distribution of the flow variables, and on the final geometry of the deposit. The input data are reported in Table 2. The same analysis at different mass flow rates is reported in the Supporting Information (S1-S2).

As showed in the previous figure, the initial Richardson number has a direct influence on the flow dynamics. For $Ri^0 = 0.5$ (Fig. 4a-d), the flow decelerates and expands more slowly (to values ranging 80 to 140 m/s, respectively for ρ_m^0 = 70.14 and 9.70 kg/m^3), beyond the first two kilometers. Instead, flows with $Ri^0 = 0.05$ (Fig. 4e-h) start with higher initial velocities, which decrease more rapidly (to values ranging 85 to 218 m/s, respectively for ρ_m^0 = 70.14 and 9.70 kg/m^3). Further, due to the effect of air entrainment, the thickness of the flow increases faster.

The dependence of the runout on the mixture density with $Ri^0 = 0.5$ is non-linear, whereas with $Ri^0 = 0.05$, the runout increases with increasing density. This trend is likely associated with non-linearity of the entrainment model. However, the net variation of the runout associated with the mixture density is much lower than that associated with the mass flow rate.

We have also analysed the influence of the initial mixture density on the final geometry of the deposit, for the same input conditions. Figure 5 shows an example of the deposit of simulated flows with different initial mixture densities for the two values of Ri^0 (0.5 and 0.05). A gradual decay in thickness with distance from the source can be observed. For both Ri, simulations show that the thickness of the deposit increases with increasing initial density, and that rapid sedimentation is observed in the first 6 km, with maximum values of 26 m, 59 m, and 140 m. Then, the thickness of the deposit decreases reaching values, at the maximum runout distance, of 0.3 m, 0.01 m and 0.02 m for $Ri^0 = 0.5$, and 1.07 m, 0.5 m and 0.016 m for $Ri^0 = 0.05$, and ρ_m^0 of 9.70 kg/m^3, 23.65 kg/m^3 and 70.14 kg/m^3, respectively (Fig. 5a and 5d).

To evaluate the influence of the initial flow density on the shape of the deposit, in Figure 5b-f we show the normalized deposit thickness (thickness/maximum thickness; expressed in log-scale) versus normalized area (area/total area), for all flow densities. The deposits show a first order exponential relationship between thickness decay and related covered area. By normalizing area and thickness with respect to their respective maximum values, the exponential fitting slope decreases with flow density (from -4.0 to -7.3 in this case – Fig. 5b), but the quality of the fit is not very good ($R^2 < 0.9$), because deposits show at least three main segments: proximal, medial and distal. To achieve a satisfactory exponential fitting, we identified an optimum region between about 0.25 and 0.75 of the normalized area, in which the fitting is exponential ($R^2 > 0.99$; Fig. 5c) and the decay rate is almost independent of the density. Upon this basis, we define proximal ($L/L_{max} < 0.25$), medial ($0.25 < L/L_{max} < 0.75$) and distal ($L/L_{max} > 0.75$) regions.

Our results are important as most of real outflow ignimbrites are well exposed in their medial regions, whereas thin distal deposits are easily eroded away and thick proximal deposits are usually buried by younger deposits or subsided during caldera collapses. This explains the exponential relationship between thickness decay and related covered area, observed for many ignimbrites (Wilson, 1991; Silleni et al., 2020).

5.3 Influence of the initial Temperature

To explore the effect of the temperature, we compared the results of three simulations at same $\dot{m}^0$ (6.82×10^{10} kg/s) and ρ_m^0 (23.65 kg/m^3) with different Ri^0 (0.5 and 0.05) and T^0 (873K, 923 K and 973 K; see Figure S4 in Supplementary Information). In Figure S4, similar trends can be observed by comparing the profiles of flow density, velocity and thickness at different T^0. Figure S4 shows that within the chosen range of initial temperatures, the overall flow dynamics and the final geometry of the deposit are rather similar, while the runout varies. In particular, flows with higher T^0 reach smaller runouts than those with lower T^0. This is because at higher temperatures, flows thermally expand more rapidly than flows at lower temperatures and therefore reach buoyancy reversal earlier.

5.4 Co-ignimbrite ash cloud

For each simulation we analysed the fractionation of the mass between the flow deposit and the co-ignimbrite ash cloud. We also computed the mass flow rate (at stationary condition) feeding the co-ignimbrite ash cloud as the ratio between the initial mass flow rate and the total deposition rate (Table S6). Table 3 reports the percentage of mass feeding the co-ignimbrite and the associated grain size distribution. Flows with $Ri^0 = 0.05$ are characterized by a much larger fractionation into the co-ignimbrite reaching more than 65% of mass compared to flows with $Ri^0 = 0.5$, which reach only 48%. Furthermore, at increasing $\dot{m}^0$ there is an increase in co-ignimbrite mass fraction. This applies to all particle sizes. In particular, it is worth noting that the percentage of the coarsest particles (1 mm and 1.6 cm) is almost independent on the mass flow rate at Ri^0=0.5 (lower air entrainment), whereas they follow the same trends of the finest particles at Ri^0=0.05 (enhanced entrainment and elutriation).

6 Application to the Pozzolane Rosse (RED) ignimbrite case study

Based upon the parametric study, we selected a narrow range of input parameters, to best fit the the runout, thickness and grain-size distribution, and temperature of the Pozzolane Rosse (RED) ignimbrite. The parametric study permits us to reconstruct two experimental curves, which show a power-law dependence of PC runout distance on initial mass flow rate $\dot{m}^0$ (Figure 6). The maximum preserved distance of the RED deposits (33 km) is a first order proxy for the PC runout. This distance intersects the experimental curves in Fig. 6 at $\dot{m}^0$ between 4.8×10^{10} and 6.8×10^{10} kg/s for flows at Ri^0 = 0.5 and $\dot{m}^0$ near 1.8×10^{11} kg/s for flows at Ri^0 0.05. To constrain the Richardson number, following laboratory experimental studies, we assume that the flow behaves as an inertial gravity current (Huppert and Simpson, 1980). We therefore limited our investigation to Ri^0=0.5, while the initial mixture density ρ_m^0 was kept variable between 9.70

and 70.14 kg/m^3. We finally fixed the initial temperature T^0 at 873K in agreement with field estimates of the ignimbrites emplacement temperature (Trolese et al. 2017). By taking the above values as a reference, we further analyzed the influence of the topography and the grain-size distribution on the flow and deposit features.

6.1 Influence of topography

We tested the effect of topography on flow dynamics by comparing propagation and depositional patterns of simulated PCs run on a flat-surface versus simulations run onto the Digital Elevation Model of the Colli Albani volcano. For both, we adopted the solid volume fractions calculated through the total grain size distribution (Supplementary information SM2). The results of the simulations with inlet mass flow rates $\dot{m}^0 = 6.82 \times 10^{10}$ kg/s are shown in Fig. 7 for three inlet mixture densities. The same analysis for $\dot{m}^0 = 4.83 \times 10^{10}$ kg/s is reported in the Supplementary information S5-S6. Fig. 7 shows the difference between the runout of the flows that propagate on the topography of the Colli Albani (solid-line) and those on a flat-surface (dashed-line). Results show that topography roughness reduces the runout. Different trends can be observed in the SW section compared to the NE section, which are characterized by different topographies: the SW sector of Colli Albani is characterized by a flat topography. Instead, the NE section has significant topographic obstacles, which comprise the caldera rim and the Apennines Mountain Range.

From our numerical results we observed a deceleration (negative peaks; Fig. 7a and c) of the flow and an increase in flow thickness (positive peaks, Fig. 7b and d) at the caldera rim and the Apennines. Additionally, the influence of topography on flow propagation increases as flow density increases. From our analysis we can conclude that uncertainty in runout not larger than 10% due to the topography can be expected.

Concerning the effect of the topography on the deposit thickness (Fig. 8), we observe different trends for denser flows (slope = -5.8°) that show a more rapid sedimentation compared to flows with same initial properties but propagating on a flat surface (slope = -4.0°). Instead, less dense flows show similar trends both on a flat and a rough topography.

6.2 Influence of the grain size distribution

We calculated the initial Total Grain Size Distribution (TGSD) of the Pozzolane Rosse ignimbrite based on the grain-size analyses of the deposit. The TGSD has been used to calculate the distribution of the simulated grain sizes ε_i as input parameters (Supplementary Information SM2).

TGSD is a difficult parameter to accurately calculate (Pioli et al., 2019), and this is so especially for ignimbrites, as the fraction of fine ash within the TGSD is certainly underestimated due to elutriation (Sparks and Walker, 1977). In addition, the common lack of very proximal exposures leads to an underestimation of the coarser particles from the TGSD. To account for uncertainties and to determine the influence of the total grain-size distribution on the runout and deposit geometry, we carried out several runs with $\dot{m}^0$ = 4.83×10^{10} kg/s and 6.82×10^{10} kg/s, $Ri^0 = 0.5$, ρ_m^0 =23.65 kg/m^3 and different particle mass fractions (n_i; Table 4). The resulting maximum runouts on the Colli Albani topography are shown in Figure 9. This set of simulations highlights how 5-10% increase or decrease in fine and coarse fractions leads to a non negligible variation in runout. In particular, it is observed that as the percentage in finer particles increases, the maximum distance reached by the flow increases.

Concerning the thickness of deposits (Fig. 10), the maximum thickness in the proximal area varies, for flow with $\dot{m}^0$ of 4.83×10^{10} kg/s, from 20.5 to 28.7 m (for ρ_m^0 =9.70 kg/m^3), from 49.5 to 56.7 m (for ρ_m^0 =23.65 kg/m^3), and from 116 to 154 m (for ρ_m^0 =70.14 kg/m^3). For flow with $\dot{m}^0$ of 6.82×10^{10}kg/s varies from 20.7 to 28 m (for ρ_m^0 =9.70 kg/m^3), from 49.6 to 66 m (for ρ_m^0 =23.65 kg/m^3), from 116.4 to 154 m (for ρ_m^0 =70.14 kg/m^3). These ranges correspond to variation of ε from 10% to 22% for d = 200 μm, from 69% to 77% for d= 1 mm and from 9% to 16% for d = 1.6 cm (Table 4). However, Fig. 10 shows that the increase or decrease of 5-10% in fine and coarse particles does not result in a significant variation of lateral decay of the thickness. The flows with ρ_m^0 =9.70 kg/m^3 (Magenta) overlap perfectly, highlighting that for these types of flows the variations on the TGSD have no effect on the deposit pattern decay, for both ṁ. The flows with ρ_m^0= 23.65 kg/m^3 show similar result as, they overlap perfectly with the exception of the distal part where small variations are observed, especially for $\dot{m}^0 = 4.83 \times 10^{10}$ kg/s. By contrast, for ρ_m^0 =70.14 kg/m^3, significant variations are observed as function of the increase in finer particles, in particular, in medial and distal area.

7 Discussion

One of the main goals of numerical modelling of pyroclastic currents is to overcome the lack of physical observations and measures from their inside, by providing key quantitative information on their internal dynamics. However, so far, several kinds of computational limitations have largely prevented the direct cross-correlation of numerical results and PCs deposits characteristics, the latter being considered as proxies for PCs dynamics. At the same time, the largest efforts in physical studies of PCs deposits have been dedicated to their local sedimentology in order to associate deposit types to the spectrum of dilute versus concentrated flows at their flow boundary (e.g. Branney and Kokelaar, 2002; Sulpizio et al. 2014). Only recently new studies have reappraised the need for global indicators, which may more properly reflect the first order transport flow dynamics. In particular, the geometry of ignimbrites, including their maximum runout and lateral thickness variations, the grain size and temperature distribution across the ignimbrite extent are considered as best indicators of mass flow rates, sedimentation and air entrainment patterns (Giordano and Doronzo 2017; Trolese et al. 2017; Palladino and Giordano, 2019; Giordano and Cas, 2021; Roche et al. 2021). At the same time, advance in computational capabilities permitted to run simulations on progressively refined grids, 3D topographies, as well as to develop improved codes for investigating fundamental processes that control PCs dynamics, such as air entrainment and sedimentation. On the basis of the results presented above, we discuss the potential of numerical modelling to reconstruct flow properties of caldera forming pyroclastic currents, constrained by their deposit's characteristics.

7.1 Runout

The results of our study highlight the dominant influence of mass flow rate on the runout (Fig. 6), in agreement with previously published models and data (Bursik and Woods, 1996; Dade and Huppert, 1996; Dufek, 2016; Shimizu et al. 2019; Roche et al. 2021; Giordano and Cas, 2021). The influence on runout of the initial Richardson number Ri^0 is negligible up to $\dot{m}^0 \approx 10^{10}$ kg/s and diverge by up to 20-25% at higher $\dot{m}^0$ (Fig. 6), showing more complex trends associated with the non-linear dependency of the entrainment coefficient on Ri (Eq. 8). In general, flows with lower Ri have shorter runouts (and larger co-ignimbrites ash cloud; Figure 11), as a result of a larger air entrainment. While it is difficult to determine the initial value of Ri from the analysis of the PC deposit, experimental data suggest that, beyond the proximal region, flows can be considered as inertial gravity currents at $Ri \sim 0.5$ (Huppert and Simpson, 1980).

Our model predicts that the TGSD has a comparable influence on PC runout with respect to $\dot{m}^0$ (Fig. 9). In the simulated scenarios, the addition of up to 10 wt. % of fine particles (Table 4) produces an increase in the runout distance of 10-15 %. This highlights the dependency of the runout on particle settling velocity (which is an increasing function of the particle diameter). Theoretically, the runout of axisymmetric currents scales with $R \sim \left(\dot{m}^0 / v_s(d_p) \right)^{0.5}$ (Dade and Huppert, 1995b), where v_s is the settling velocity and d_p is diameter of the particles. From the statistical analysis of dilute PCs runout data, Roche et al. (2021) found:

$$R = 12 \times 10^{-4} \left(\dot{m}^0 / v_s(d_p) \right)^{0.484} \qquad \text{eq. 15}$$

which is close to the theoretical law and sets the proportionality factor. Analysis of our numerical results data of Figure 6 leads to the following fit:

$$R = 3.6 \times 10^{-4} \left(\dot{m}^0 / v_s(d_p) \right)^{0.484} \qquad \text{eq. 16}$$

The difference with eq. (15) can be related to multiple factors, which need more study to be fully solved. First, in our simulation we consider the total mass flow rate, which includes PC and co-ignimbrite, while Roche et al. (2021) consider the average $\dot{m}^0$ values only for the PC. As a second difference, the estimates by Roche et al. consider only one single (mean) grain size, while we consider the compound effect of a polydisperse (three-phases) mixture. It is questionable whether the mean grain size can approximate a polydisperse mixture (Bonnecaze et al., 1996), however it is clear that the choice of the particle size can significantly change the predictions from Eq. (15). Both factors act in the direction of reducing the scaling factor in Eq. (15). In any case, the theoretical trend is confirmed also by our results.

Finally, the initial temperature also affects the flow runout, by less than 20% in the simulated range (Fig. S4 in Supplementary Information)

7.2 Deposit thickness decay patterns

The results of numerical simulations at fixed $\dot{m}$ suggest that the sensitivity of the runout to initial mixture density is smaller than that to the mass flow rate (Fig. 4). On the contrary, the initial mixture density (or particle concentration) has a clear influence on the geometry of the deposit. The data obtained in this study permit us to establish a relation between the deposit thickness decay pattern and the initial mixture flow density, at fixed total grain size parameters (Fig 5a; Fig. 8a): denser flows tend to have a higher sedimentation rate in the proximal area compared to initially less dense flows. This deposit pattern is caused by the effect of density on sedimentation, which in turns has an effect on co-ignimbrite partitioning. Lower-density flows, characterized by higher speeds than high density flow, have greater air entrainment, with a consequent downflow increase in flow thickness (Fig. 7b and 7f). As a consequence, more material is conveyed into the co-ignimbrite.

Thickness decay patterns for a limited though representative number of deposits of large-volume flows have recently been shown to have first-order exponential decays with distance (Silleni et al. 2020). BW96 qualitatively suggested that such decay patterns could reflect flow properties. We have defined at least three regions of sedimentation: proximal, up to 0.25 of the runout; medial, between 0.25 and 0.75; and distal from 0.75 to final runout. The medial region, which is the most exposed in real ignimbrites, shows a well-defined exponential thinning pattern (Fig. 5c,f; Fig. 8c). In particular, as shown in Fig. 5 and 8, flows with higher density are characterized by a ratio between proximal and medial thickness much larger than dilute ones, associated with more rapid sedimentation in the proximal part. On this basis, we suggest that it might be possible to have information about the PC density from the ratio between the proximal and the medial thickness, e.g., the value of the normalized deposit at one fourth of the runout. Moreover, results show that the initial temperature does not affect significantly the geometry of the deposit.

7.4 Co-ignimbrite ash cloud

Regarding the percentage of the particles conveyed into the co-ignimbrite ash cloud, our study highlights a clear increasing trend with the mass eruption rate (Fig. 11), with the percentage of elutriated fine particles attaining 90% for the highest mass eruption rates and lowest Ri^0 investigated. This result highlights once more the difficulty in reconstructing the total grain size distribution from the PC deposits. In addition, considering the final velocities reached by the flows at the maximum runout (from 127 to 61 m/s for Ri^0 =0.5 and from 214 to 84 m/s for

Ri^0 =0.05), it can be deduced that flows still retain a significant momentum at liftoff distance (Fig. 4a,e). This implies that the grain-sizes that can be conveyed into the coignimbrite cloud are not limited to elutriated fine-ash, but can potentially include lapilli-to bomb-sized particles. In essence, co-ignimbrites ash cloud forming at maximum runout may have local conditions to become root-less vertical columns, which may resemble Plinian columns. A detailed study of the grain-size distribution of co-ignimbrite deposits may provide essential (and so far under-explored) field data sets to constrain flow dynamics of the parent flows.

7.5 The Pozzolane Rosse (RED) ignimbrite: reconstruction of source and flow properties

The study presented here aims at reconstructing the dynamics of a PC capable of generating a deposit similar to the Pozzolane Rosse ignimbrite (RED). The maximum distance of RED deposits in outcrop is about 33 km from the centre of the caldera (Giordano and Dobran, 1994 and Giordano et al., 2010), in the SW direction. In addition, the RED ignimbrite is found across the Apennine Mountains ridge where it is valley confined and reaches preserved maximum distance of more than 30 km. Based on the parametric analysis, the best selection of input parameters to match runout and deposit characteristics of RED are flows with $\dot{m}^0$ = 6.8×10^{10} kg/s; T^0 = 873 K; Ri^0 = 0.5. Error on the mass flow rate can be estimated to be around 20% considering both uncertainties associated with the grain-size and topography.

We notice that the mass flow rate selected in our study is one order of magnitude larger than that used by Giordano and Dobran (1994). Those authors assumed a simple cylindrical vent and adopted the maximum mass flow rate permitted for such configuration. However, numerical simulations in that range could neither match the RED maximum runout, nor the overpassing of the Apennine Monutains ridge. Our hypothesis of a higher mass flow rate might be compatible by an eruption fed by a caldera ring fault, rather than a single vent (Giordano and Cas, 2021).

In our simulation a 28 km runout can be observed in SW section. However, simulations with a 10% increase in the fine particles content resulted in an increase in the distances reached, allowing flows with an intermediate initial density (ρ_m^0 = 23.65 kg/m^3) to reach a runout of 30 km. The difference of 5 km as the grain size changes, highlights the key role of grain size distribution as input parameter and, in particular, the role of finer particles in controlling the runout. Furthermore, it suggests that the uncertainty on the grain-size becomes an uncertainty about the mass flow rate, as an increase in the fine fraction (as usually reasonable due to the common underestimation of the co-ignimbrite fractionation) leads to an increase in the flow runout (see section 6.2). The main topographic obstacle is represented by the Apennines to the northeast and southeast of the caldera (Fig 1). To note, in the eastward sector PCs are channelled into the valley between the two Apennines. Here runouts reach the maximum distances. In all simulations the flows are able to reach elevations above 600 m, with the exception of the flow with the highest initial density (ρ_m^0= 70.14 kg/m^3 - under 400m of height).

7.5.1 Total Grain Size Distribution

The grain-size distribution has an important effect on both the simulated runout and deposit thickness and it is worth remarking that the uncertainty in TGSD reflects on the uncertainty in the reconstructed mass flow rate. However, our results, for equal TGSD, show that the simulated and real grain-size distribution in the resulting deposits are similar for initial flow densities ρ_m^0 of 9.70 kg/m^3 and 23.65 kg/m^3. In these flows, all three modelled grain-sizes are present for the full extent of the flow (~ 33 km), as observed in the field data (Rosa, 1987). For higher concentration flows, with an initial density of 70.14 kg/m^3, the simulated and real grain-size are similar only up to 10 km from source. Simulations indicate that, farther than 10 km, the denser flow is characterized only by the smallest grain-sizes (i.e. 1 mm and 200 μm), whereas in the RED case study the coarse fraction is ubiquitously present. This difference is also observed in the flat topography simulations, suggesting that these trends are related to flow processes and in particular to a higher sedimentation rate in denser flows.

7.5.2 Deposit thickness

The exponential thickness decay shown by our numerical simulations (Figure 12a) is typical also of many other large volume ignimbrites (Silleni et al., 2020). In Figure 12b we compare the thickness of the simulated deposits with that of the RED deposit and of other ignimbrites, as a function of the deposit area. The data represent flows with 10% more fine particles (green dashed-line in the figure), with runouts comparable to those in nature (black solid-line). In addition, we consider a final thickness of 1 m, since the distal part of the flow does not have exponential trend, (see section 5.2).

Simulated flows have equal duration and mass flow rate, but they can have different deposit volumes, because of their different sedimentation rate and partitioning in the co-ignimbrite ash cloud. By increasing the simulation duration, the exponential fitting line increases its slope, however the runout does not change. Such behaviour points to a flow scenario with lower density, i.e., a thick and dilute flow. Although the modelling and subsequent comparison of multiple ignimbrites is beyond the scope of the paper, thanks to Silleni et al. (2020) we are able to do an indirect comparison (please refer to figure 12a). The comparison suggests that our findings could likely be generalized to all PCs of this type.

7.5.3 A flow scenario for the Pozzolane Rosse (RED) ignimbrite

The discussion of the numerical results constrained by field data of the RED ignimbrite reconstructs a well-defined scenario characterised by initial mass flow rates in the order of 6.8 × 10^{10} kg/s, Ri^0= 0.5, initial average density between 9.70 kg/m^3 and 23.65 kg/m^3 and a TGSD similar to that of the real ignimbrite, with up to 10% higher finest fraction. This scenario does not overlap with other combinations of the selected input parameters and permits us to explain the first order deposit characteristics of the RED ignimbrite, i.e. the axisymmetic distribution of the ignimbrite across highly variable topography, the maximum distance at which the ignimbrite is found and the maximum elevations climbed (Giordano and Dobran, 1994), the thickness decay with distance (Giordano and Doronzo, 2017), the grain size distribution along the areal dispersal (Rosa, 1987), and the minimal drop of the temperature of emplacement from source to maximum runout (Trolese et al., 2017). Such a complete dataset has so far never been inverted by PCs numerical simulations and we stress its relevance for future studies.

The excellent agreement between first order descriptors of the RED ignimbrite and simulated flow parameters suggests that the largest part of the mass was transported within a dilute flow, which can be well approximated by a depth-averaged model and whose dynamics were largely unaffected by the high concentration undercurrent.

By adopting a depth-averaged model, we have disregarded the internal stratification of the flow and therefore we cannot comment on flow boundary processes occurring in the basal high concentration layer and the resulting ignimbrite lithofacies architecture. These flow boundary processes may be better investigated with two-layer models for pyroclastic currents (Kelfoun, 2017; Shimizu et al., 2019). However we stress that our results show that, unless the analysed ignimbrite shows evidence for significant decoupling of the basal undercurrent and its ability to flow far distances independently (e.g. Druitt et al. 2002), a one-layer depth-averaged model is appropriate for investigating the first order transport and depositional characteristics of ignimbrites. To clarify, our model applies to ignimbrites that owe the areal distribution of their mass (here measured in terms of distribution of thickness and grain size) largely to transport processes occurring in the dilute portion of the current, irrespectively of the local lithofacies which is instead largely controlled by the mode of deposition of the basal high concentration layer.

In tha case of the RED ignimbrite, its mass radial distribution at first order reflects the transport processes within the dilute current, as well as the grain-size and temperature of pyroclasts, all only minimally (at the scale of the ignimbrite) redistributed by the basal undercurrent as a function of its the interaction with the local topography. For example, the depositional facies of RED ignimbrite are almost uniformly massive and valley-pond where confined the mountain areas, characteristics that are typically related to high concentration flows (Giordano and Doronzo, 2017; Smith et al., 2020). There are many similar cases, such as The Campanian Ignimbrite (Silleni et al., 2020), the Ito ignimbrite (Bear et al., 1997) and the Taupo ignimbrite (Roche et al., 2021), where the ignimbrite show characteristics typical of deposits from concentrated flows but their axisymmetric dispersal and runout, thickness and grain-size lateral decay pattern, and low aspect ratio suggest transport from dilute current. According to our results, the characteristic ofthe RED case study may be valid for many of the PCs related to large scale caldera forming ignimbrites (Roche et al., 2021; Giordano and Cas, 2021).

In this respect, we notice that the depositional characteristics of some large volume caldera forming ignimbrites such as the Cerro Galan ignimbrite (Cas et al., 2011) and the Peach Spring Tuff (Roche et al., 2016) have been used to infer slow-moving and far reaching dense pyroclastic flows. As these ignimbrites also share the first order geometry and distribution of the investigated case study, we caution on the possibility that the amount of mass and its grain size delivered at each locality may reflect at first order the transportation in an upper dilute current.

8 Conclusions

In this paper, we proposed a model in which the ignimbrite characteristics are mainly controlled by transport by an inertial current. We have demonstrated that our approach based on a single-layer, depth-averaged model can be used to simulate the propagation of inertial PC and their deposits inaldera settings,for a wide range of mass flow rates, densities and volume particle concentrations. Numerical simulations permitted us to quantify the effects of atmospheric air entrainment by varying the initial Richardson number (Ri^0), and of the initial flow thickness, initial flow velocity and mixture density on runout and thickness decay pattern.

The runout, the grain-size distribution, and the temperature obtained from the field data have been used as input parameters for the numerical model. The model produces several outputs that can be directly compared with the deposit features, such as runout, thickness decay patterns, grain-size distribution and temperature as a function of the radial distance from source, as well as a quantification of the mass partitioned into the co-ignimbrite. The results of the simulations proved to be consistent with the characteristics of the deposits.

Two fundamental results arise from our study: first, the runout is primarily controlled by the mass flow rate (in agreement with previous studies). Second, the thickness decay pattern is primarily controlled by the average flow density (or the flow particle concentration) and total grain-size distribution. Reconstruction of both observables requires a careful characterization of the total grain-size distribution in the flow, which also has a first-order influence on the runout. By using the numerical model, it is thus possible to invert the deposit data to reconstruct the initial PC parameters.

Acknowledgments

Many thanks to Biagio Giaccio (CNR-IGAG) for introducing us to the distal co-ignimbrite deposits of the Pozzolane Rosse. The authors thank two anonymous reviewers and the asscociated editor (O. Roche) for comments and suggestions that helped to improve this manuscript, and the editor for editiorial handling of the manuscript. L. C. gratefully acknowledges a Ph.D. grant from INGV and the Department of Sciences, Roma Tre University (MIUR-Italy Dipartimenti di Eccellenza, ARTICOLO 1, COMMI 314–337 LEGGE 232/2016). The authors declare no conflicts of interest. The data archiving is underway on Figshare (the following DOI will become active when the item is published).

Figures Captions

Figure 1: Dispersal area of the pyroclastic current deposits with the location of the sampling. a: DEM of the Colli Albani volcano showing the main morphostructural of volcano and locations of the sampling of Rosa (1987); b: Stratigraphic section of the RED units; c: RED flow unit succession at Via Fioranello (Esman quarry; coord. UTM: 296735 m E – 4628775.64 m N), at 9 km WNW from the Colli Albani caldera rim. RED is more than 15 m thick and is altered to a thick palaeosoil at the top; d: Typical massive and chaotic lithofacies of the RED ignimbrite (via Fioranello).

Figure 2: Schematic illustration of the gravity current. This configuration represents the radial injection of the multiphase flow mixture from a cylindrical structure. Arrows indicate direction of flow.

Figure 3: **Influence of mass flow rate on flow propagation**. Representative numerical results of five flow at different $\dot{m}^0$ (10^9 – 10^{10} kg/s) with two Ri^0: 0.5 (left) and 0.05 (right) and same initial mixture density (ρ_m^0 =23.65 kg/m^3) along radial distance. Variation of flow velocity (a and e); flow thickness (b and f); density (c and g) and temperature (d and h) as a function of the distance from the source. (For interpretation of colours see legend in figure).

Figure 4: Influence of initial flow density on flow propagation. Representative numerical results of three flow with different initial mixture densities (9.70, 23.65 and 70.14 kg/m^3) with two Ri^0 and same $\dot{m}^0$ (6.82×10^{10}kg/s) along radial distance. Ri^0 = 0.5: left and Ri^0 = 0.05: right. Variation of velocity (a and e); thickness (b and f); density (c and g) and temperature (d and h) as a function of the distance from the source. (For interpretation of colours see legend in figure).

Figure 5: **Influence of initial flow density on shape of the deposit**. a-d: Thickness of deposits versus distance from source along East direction. b-e: Normalized thickness (thickness/maximum thickness in log scale) versus normalised area (area/total area) of three flow at different initial mixture density ρ_m^0: 9.70 kg/m^3 (Magenta line) 23.65 kg/m^3 (Green line) and 70.14 kg/m^3 (Red line) with two Ri^0 (0.5 and 0.05) and same $\dot{m}^0$ (6.82×10^{10}kg/s). c-f: interval between 0.25 and 0.75 in which the thickness decreases along with increasing areas with an exponential trend. Dashed line represents the trendline.

Figure 6: Relationships for PC runout distance as a function of the initial mass flow rate. Runout distance (in log-scale) as a function of mass flow rate ($\dot{m}^0$; in log-scale). The difference in runout arises owing to the difference in air entrainment rate between Ri^0 = 0.5 (in blue) and Ri^0 = 0.05 (in red). Black dashed lines represent the fit-line for Ri^0 = 0.5 with a coefficient of R^2 = 0.996. Black solid line represent the fit-line for Ri^0 =0.05 with a coefficient of R^2 = 0.999.

Figure 7: Influence of topography on flow dynamic. Representative numerical results of three flow with different initial mixture densities ρ_m^0 (9.70, 23.65 and 70.14 kg/m^3) with Ri^0= 0.5 and $\dot{m}^0$ (6.82×10^{10} kg/s) along SW – NE section. Variation of flow velocity (a); flow thickness (b) as a function of the distance. Topography: Solid line; Flat-surface: Dashed line. Magenta: 9.70 kg/m^3; Green: 23.65 kg/m^3; Red: 70.14 kg/m^3.

Figure 8: **Influence of initial flow density on the shape of the deposit** a: Thickness of deposits versus distance from source along East direction of three flow at different initial mixture densities ρ_m^0: 9.70 kg/m^3 (Magenta line) 23.65 kg/m^3 (Green line) and 70.14 kg/m^3 (Red line) with Ri^0=0.5 and $\dot{m}^0$ (6.82×10^{10} kg/s). b: Normalized thickness (thickness/maximum thickness in log scale) versus normalized area (area/total area). c: Interval between 0.25 and 0.7 of normalized area in which the thickness decreases along with increasing areas with an exponential trend. Black dashed line represents the trendline.

Figure 9: **Inundation area of the simulations at different TGSD**. Representative numerical results of a flow with initial mixture density ρ_m^0 23.65 kg/m3 and $Ri^0 = 0.5$. a: $\dot{m}^0$= 4.83×10^{10} kg/s; b: $\dot{m}^0$= 6.82×10^{10} kg/s. Green line:

TGSD values; Blue: TGSD values + 5% (dashed) and + 10% (densely dashed) in fine particles; Red: TGSD values + 5% (dashed) and + 10% (densely dashed) in coarse particles. Coordinates are expressed in the UTM cartographic system.

Figure 10: Influence of TGSD on shape of the deposit. Normalized thickness (thickness/maximum thickness in log scale) versus normalized area (area/total area) of five flow with two different $\dot{m}^0$ at Ri^0 = 0.5 and different TGSD. a: 4.83×10^{10} kg/s; b: 6.82×10^{10} kg/s The flows with ρ_m^0= 9.70 kg/m^3 (Magenta) overlap perfectly, highlighting that for these types of flows the variations on the TGSD have no effect on the deposit pattern decay. The flows with $\rho_m^0 = 23.65$ kg/m^3 (Green) as for the less dense ones, they overlap perfectly with the exception of the distal part where small variations are observed. The flows with ρ_m^0 = 70.14 kg/m^3 (Red) show a variation in the geometry of the deposit caused by the different TGSDs adopted. In particular, it can be observed that flows with a higher percentage of fines (10%, densely dashed line) tend to have a lower proximal to distal thickness ratio than the other TGSDs.

Figure 11: Relationships for co-ignimbrite as a function of mass flow rate. Mass fraction into the co-ignimbrite ash cloud (expressed in percentage) as a function of mass flow rate ($\dot{m}^0$ in log-scale). The difference in mass fraction arises owing to the difference in air entrainment rate between Ri^0 =0.5 (in blue) and Ri^0 = 0.05 (in red). The simulations corresponded to a current with T^0 = 873 K and ρ_m^0 = 23.65 kg/m^3.

Figure 12: Comparison beween simulations and actual deposits. a: Thickness (in log scale) vs. area enclosed in that thickness of each isopach for different ignimbrites [Lund Ignimbrite in red; Greens Canyon Tuff in green, Oruanui Ignimbrite in blue; Campanian Ignimbrite in orange; Petroglyph Cliff in black; and the Pozzolane Rosse Ignimbrite in purple]. The dashed lines represent the fit for each ignimbrite. The plotted points are those obtained by the isopach map (modiefied from Silleni et al., 2021). b:Thickness (in log-scale) vs. the area of each isopach of the Pozzolane Rosse Ignimbrite (RED) show by black dots. The black solid line represents the exponential trend of RED (Giordano and Doronzo, 2017). The dashed lines represent the exponential tren of simulated flows at $\dot{m}^0$ = 6.82×10^{10} kg/s with ρ_m^0 = 70.14kg/m^3 in red; ρ_m^0 = 23.65 kg/m^3 in green and ρ_m^0 = 9.70 kg/m^3 in magenta.

References

Andrews, B. J. (2014). Dispersal and air entrainment in unconfined dilute pyroclastic density currents. Bulletin of Volcanology, 76(9), 1-14.

Báez, W., Bustos, E., Chiodi, A., Reckziegel, F., Arnosio, M., de Silva, S., ... & Peña-Monné, J. L. (2020). Eruptive style and flow dynamics of the pyroclastic density currents related to the Holocene Cerro Blanco eruption (Southern Puna plateau, Argentina). Journal of South American Earth Sciences, 98, 102482

Benjamin, T. B. (1968). Gravity currents and related phenomena, J. FluidMech., 31, 209 – 248

Best, M. G., Gromme, S., Deino, A. L., Christiansen, E. H., Hart, G. L., & Tingey, D. G. (2013). The 36–18 Ma central Nevada ignimbrite field and calderas, Great Basin, USA: multicyclic super-eruptions. Geosphere 9, 1562–1636. doi:10.1130/GES00945.1

Bignami, C., Runch, J., Chini, M., Neri, M., Buongiorno, M.F., Hidayati, S., Sri Sayudi, D. & Surono. 2013. Pyroclastic density current volume estimation after the 2010 Merapi volcano eruption using X-band SAR. Journal of Volcanology and Geothermal Research. DOI: 10.1016/j.jvolgeores.2013.03.023.

Boari, E., Avanzinelli, R., Melluso, L., Giordano, G., Mattei, M., De Benedetti, A.A., Morra, V. & Conticelli, S. (2009). Isotope geochemistry (Sr–Nd–Pb) and petrogenesis of leucite-bearing volcanic rocks from "Colli Albani" volcano, Roman Magmatic Province, Central Italy: inferences on volcano evolution and magma genesis. Bulletin of Volcanology, 71(9), 977-1005.

Bonnecaze, R.T., Huppert, H.E., & Lister, J.R. (1996). Patterns of Sedimentation from Polydispersed Turbidity Currents. Proceedings of the Royal Society a: Mathematical, Physical and Engineering Sciences, 452(1953), 2247–2261. http://doi.org/10.1098/rspa.1996.0120.

Branney, M. J., & Kokelaar, P. (2002). Pyroclastic density currents and the sedimentation of ignimbrites. In Geological Society Memoir No. 27. (Ed.), 27 (Issue 2). https://doi.org/http://doi.org/10.1086/427850.

Breard, E.C.P. & Lube, G.(2017) Inside pyroclastic density currents – uncovering the enigmatic flow structure and transport behaviour in large-scale experiments. Earth Planet. Sci. Lett. 458, 22–36.

Brown, R. J. & Andrews, G. D. (2015). Deposits of pyroclastic density currents, in Encyclopedia of volcanoes. 2nd Edn, Editors Sigurdsson, H., Houghton, B.F., Mcnutt, S., Rymer, H. and J. Stix (San Diego, CA: Academic Press), 631–648.

Bürger, R. & Wendland, W.L. (2001). Sedimentation and suspension flows: Historical perspective and some recent developments. Journal of Engineering Mathematcis, 41(2-3):101.116.

Burgisser, A. & Bergantz, G. (2002). Reconciling Pyroclastic Flow and Surge: the Multiphase Physics of Pyroclastic Density Currents. Earth and Planetary Science Letters. 202. 405-418. 10.1016/S0012-821X(02)00789-6.

Bursik, M. I. & Woods, A. W. (1996). The dynamics and thermodynamics of large ash flows. Bulletin of Volcanology, 58(2–3), 175–193. https://doi.org/10.1007/s004450050134.

Calvari, S.; Di Traglia, F.; Ganci, G.; Giudicepietro, F.; Macedonio, G.; Cappello, A.; Nolesini, T.; Pecora, E.; Bilotta, G.; Centorrino, V.; Corradino, C.; Casagli, N.; Del Negro, C. (2020). Overflows and Pyroclastic Density Currents in March-April 2020 at Stromboli Volcano Detected by Remote Sensing and Seismic Monitoring Data. Remote Sens. 12, 3010. https://doi.org/10.3390/rs12183010.

Campagnola, S., Vona, A., Romano, C. & Giordano, G. (2016). Crystallization kinetics and rheology of leucite-bearing tephriphonolite magmas from the Colli Albani volcano (Italy). Chemical Geology, 424, 12-29.

Cas, R.A.F., Wright, H.M.N., Folkes, C.B., Lesti, C., Porreca, M., Giordano, G.& Viramonte, J.G. (2011). The flow dynamics of an extremely large volume pyroclastic flow, the 2.08-Ma Cerro Galán Ignimbrite, NW Argentina, and comparison with other flow types. Bull Volcanol 73, 1583–1609. https://doi.org/10.1007/s00445-011-0564-y.

Cas, R.A.F., & Wright, J.V., 1987. Volcanic Successions: Modern and Ancient. Allen and Unwin.

Chiodini, G. & Frondini, F. (2001). Carbon dioxide degassing from the Albani Hills volcanic region, Central Italy. Chemical Geology, 177(1-2), 67-83.

Cole, P. D., Calder, E. S., Sparks, R. S. J., Clarke, A. B., Druitt, T. H., Young, S. R., ... & Norton, G. E. (2002). Deposits from dome-collapse and fountain-collapse pyroclastic flows at Soufrière Hills Volcano, Montserrat. Geological Society, London, Memoirs, 21(1), 231-262.

Conticelli, S., Boari, E., Avanzinelli, R., De Benedetti, A. A., Giordano, G., Mattei, M., Melluso, L & Morra, V. (2010). Geochemistry, isotopes and mineral chemistry of the Colli Albani volcanic rocks: constraints on magma genesis and evolution. In The Colli Albani Volcano (Vol. 3, pp. 107-139). Geological Society of London, Special Publications of IAVCEI.

Dade, W. B. (2003). The emplacement of low-aspect ratio ignimbrites by turbulent parent flows. Journal of Geophysical Research: Solid Earth, 108(B4), 1–9. https://doi.org/10.1029/2001jb001010.

Dade WB & Huppert HE (1996). Emplacement of the Taupo ignimbrite by a dilute turbulent flow. Nature 381:509–512.

Dade, W. B. & Huppert, H. E. (1995b). A box model for non-entraining, suspension-driven gravity surges on horizontal surfaces. Sedimentology 42 (3), 453-470.

Dade, W. B. & Huppert, H. E. (1995a). Runout and fine-sediment deposits of axisymmetrical turbidity currents. J. Geophys. Res. 100:18597–609.

Dade, W.B., Lister, J.R. & Huppert, H.E. (1994). Fine-sediment deposition from gravity surges on uniform slopes. J. Sediment. Res. A 64:423–32.

Dellino, P., Dioguardi, F., Doronzo, D.M. & Mele, D. (2019). The rate of sedimentation from turbulent suspension: An experimental model with application to pyroclastic density currents and discussion on the grain-size dependence of flow runout. Sedimentology, 66: 129-145. https://doi.org/10.1111/sed.12485.
Dellino, P., Zimanowski, B., Buttner, R., La Volper, L., Mele, D. & Sulpizio, R. (2007). Large-scale experiments on the mechanics of pyroclastic flows: design, engineering, and first results. J. Geophys. Res. Solid Earth 112, B04202.
De'Michieli Vitturi, M., Esposti Ongaro, T., Lari, G., &Aravena, A. (2019). IMEX-SfloW2D 1.0: A depth-averaged numerical flow model for pyroclastic avalanches. Geoscientific Model Development, 12(1), 581–595. https://doi.org/10.5194/gmd-12-581-2019.
Doronzo, D.M. (2012). Two new end members of pyroclastic density currents: Forced convection-dominated and inertia-dominated. Journal of Volcanology and Geothermal Research, 219–220, 87–91. https://doi.org/10.1016/j.jvolgeores.2012.01.010.
Doronzo, D. M., Giordano, G., & Palladino, D. M. (2021) Energy facies: a global view of pyroclastic currents from vent to deposit. Terra Nova. https://doi.org/10.1111/ter.12561.
Doyle, E.E., Hogg, A.J., Mader, H.M. & Sparks, R.S.J. (2010). A two-layer model for the evolution and propagation of dense and dilute regions of pyroclastic currents. J Volcanol Geotherm Res 190:365–378. https://doi.org/10.1016/j.jvolgeores.2009.12.004.
Druitt, T.H., Calder, E.S., Cole, P.D., Hoblitt, R.P., Loughlin, S.C., Norton, G.E., Ritchie, L.J., Sparks, R.S.J. & Voight, B. (2002). Small-volume, highly mobile pyroclastic flows formed by rapid sedimentation from pyroclastic surges at Soufrière Hills Volcano, Montserrat: an important volcanic hazard. Memoirs-Geological Society of London, 21, 263-280.
Druitt, T. H. (1998). Pyroclastic density currents. Geological Society Special Publication, 145, 145–182. https://doi.org/10.1144/GSL.SP.1996.145.01.08.
Dufek, J. (2016). The Fluid Mechanics of Pyroclastic Density Currents. Annual Review of Fluid Mechanics, 48(September), 459–485. https://doi.org/10.1146/annurev-fluid-122414-034252.
Dufek, J. & Bergantz, G. W. (2007). Dynamics and deposits generated by the Kos Plateau Tuff eruption: Controls of basal particle loss on pyroclastic flow transport. Geochem. Geophys. Geosyst. 8, Q12007 .
Ellison, T. H. & J. S. Turner (1959). Turbulent entrainment in stratifiedflows, J. Fluid Mech., 6, 423 – 448
Esposti Ongaro, T., Komorowski, J.C., Legendre, Y. & Neri, A. (2020). Modelling pyroclastic density currents from a subplinian eruption at La Soufrière de Guadeloupe (West Indies, France). Bulletin of Volcanology, 82(12). https://doi.org/10.1007/s00445-020-01411-6.
Esposti Ongaro, T., Orsucci, S. & Cornolti, F. (2016). A fast, calibrated model for pyroclastic density currents kinematics and hazard. Journal of Volcanology and Geothermal Research, 327, 257–272. https://doi.org/10.1016/j.jvolgeores.2016.08.002.
Esposti Ongaro, T., Clarke, A.B., Voight, B., Neri, A. & Widiwijayanti, C., (2012). Multiphase flow dynamics of pyroclastic density currents during the May 18, 1980 lateral blast of Mount St. Helens (USA). J. Geophys. Res. 117, B06208. http://dx.doi.org/10.1029/2011JB009081.
Esposti Ongaro, T., Widiwijayanti, C., Clarke, A. B., Voight, B. & Neri, A. (2011). Multiphase-flow numerical modeling of the 18 May 1980 lateral blast at Mount St. Helens, USA. Geology 39, 535–538.
Esposti Ongaro, T., Neri, A., Menconi, G., de' Michieli Vitturi, M., Marianelli, P. , Cavazzoni, C. , Erbacci G. & Baxter P. J., (2008). "A transient 3D numerical simulation of column collapse and pyroclastic flow scenarios at Vesuvius", J. Volcanol. Geotherm. Res. 178.
Fauria, K. E., Manga, M. & Chamberlain, M. (2016). Effect of particle entrainment on the runout of pyroclastic density currents. J. Geophys. Res. Solid Earth 121, 6445–6461.
Fisher, R.V. (1995). Decoupling of pyroclastic currents: hazards assessments. Journal of Volcanology and Geothermal Research. 66- 1- 257- 263- 1995. SN - 0377-0273. DOI: https://doi.org/10.1016/0377-0273(94)00075-R .
Fisher, R. V., Orsi, G., Ort, M. & Heiken, G. (1993). Mobility of a large-volume pyroclastic flow - emplacement of the Campanian ignimbrite, Italy. Journal of Volcanology and Geothermal Research, 56(3), 205–220. https://doi.org/10.1016/0377-0273(93)90017-L.Freda, C., Gaeta, M., Giaccio, B., Marra, F., Palladini, D.M., Scarlato, P. & Sottili, G. (2011). CO2-driven large mafic explosive eruptions: the Pozzolane Rosse case study from the Colli Albani Volcanic District (Italy). Bull Volcanol 73, 241–256. https://doi.org/10.1007/s00445-010-0406-3
Geyer, A. & Marti, J. (2014). A short review of our current understanding of the development of ring faults during collapse caldera formation. Frontiers in Earth Science. 2. 10.3389/feart.2014.00022.
Giaccio, B., Arienzo, I., Sottili, G., Castorina, F., Gaeta, M., Nomade, S., Galli, P. & Messina, P. (2013). Isotopic (Sr–Nd) and major element fingerprinting of distal tephras: an application to the Middle-Late Pleistocene markers from the Colli Albani volcano, central Italy. Quaternary Science Reviews, 67, 190–206. https://doi.org/10.1016/J.QUASCIREV.2013.01.028.
Giordano, G. (1998). The effect of paleotopography on lithic distribution and facies associations of small volume ignimbrites: The WTT Cupa (Roccamonfina volcano, Italy). Journal of Volcanology and Geothermal Research, 87(1–4), 255–273. https://doi.org/10.1016/S0377-0273(98)00096-1.
Giordano, G. & Cas, R. (2021). Classification of ignimbrite and thei eruptions. Earth-Science Reviews 220 (2021) 103697. https://doi.org/10.1016/j.earscirev.2021.103697
Giordano, G. & Dobran, F. (1994). Computer simulations of the Tuscolano Artemisio's second pyroclastic flow unit (Alban Hills, Latium, Italy). Journal of Volcanology and Geothermal Research, 61(1–2), 69–94. https://doi.org/10.1016/0377-0273(94)00013-1.
Giordano, G. & Doronzo, D.M. (2017). Sedimentation and mobility of PDCs: A reappraisal of ignimbrites' aspect ratio.

Scientific Reports, 7(1), 1–7. https://doi.org/10.1038/s41598-017-04880-6.

Giordano, G., De Benedetti, A.A., Diana, A., Diano, G., Esposito, A., Fabbri, M., Gaudioso, F., Marasco, F., Mazzini, I., Miceli, M., Mincione, V., Porreca, M., Rodani, S., Rosa, C., Vinkler, A.P., Caprilli, E., Taviani, S., Trigari, A., Bilardello, D., Malinconico, S., Sabato Ceraldi, T., Funiciello, R., Mattei, M., De Rita, D., Parotto, M. & Cas, R.A.F. (2010). Stratigraphy and volcano-tectonic structures of the Colli Albani volcanic field. In: Funiciello, R., Giordano, G. (Eds.), The Colli Albani Volcano. In: Special Publication of IAVCEI, vol.3. The Geological Society, London, pp.43–97.

Giordano, G., De Benedetti, A. A., Diana, A., Diano, G., Gaudioso, F., Marasco, F., Miceli, M., Mollo, S., Cas, R.A.F. & Funiciello, R. (2006). The Colli Albani mafic caldera (Roma, Italy): Stratigraphy, structure and petrology. Journal of Volcanology and Geothermal Research, 155(1–2), 49–80. https://doi.org/10.1016/j.jvolgeores. 2006.02.009.

Gueugneau, V., Kelfoun, K., Roche, O. & Chupin, L. (2017). Effects of pore pressure in pyroclastic flows: Numerical simulation and experimental validation. Geophysical Research Letters, 44 (5), p. 2194-2202. ISSN 0094-8276.

Huppert, H. E. & J. E. Simpson (1980). The slumping of gravity currents,J. Fluid Mech., 99, 785 –799

Kelfoun, K. (2017). A two-layer depth-averaged model for both the dilute and the concentrated parts of pyroclastic currents. Journal of Geophysical Research: Solid Earth, 122(6), 4293–4311. https://doi.org/10.1002/2017JB014013.

Kelfoun K., Samaniego P.P. & Barba D. (2009) Testing the suitability of frictional behaviour for pyroclastic flow simulation by comparison with a well-constrained eruption at Tungurahua volcano (Ecuador). Bull Volcanol 71(9):1057–1075.

Kelfoun K. & Druitt T.H., (2005) Numerical modeling of the emplacement of Socompa rock avalanche, Chile. J Geophys Res 110:B12202. doi:10.1029/2005JB003758.

Kieffer, S.W. & Sturtevant, B. (1984). Laboratory studies of volcanic jets. Journal of Geophysical Research 89: doi: 10.1029/JB080i010p08253. issn: 0148-0227.

Lesti, C., Porreca, M., Giordano, G., Mattei, M., Cas, R.A.F., Wright, H. & Viramonte, J., 2011. High temperature emplacement of the Galán and Toconquis Group ignimbrites (Puna plateau, NW Argentina) determined by TRM analyses. In: Cas RAF, Cashman K (eds) The Cerro Ignimbrite and Caldera: characteristics and origins of a very large volume ignimbrite and its magma system. Bulletin of Volcanology, 73, 1535

Lube, G., Breard, E. C. P., Esposti-Ongaro, T., Dufek, J. & Brand, B. (2020). Multiphase flow behaviour and density currents. Nature Reviews Earth and Environment, June. https://doi.org/10.1038/s43017-020-0064-8.

Lube, G., Breard, E.C.P., Cronin, S.J. & Jones, J. (2015). Synthesizing large-scale pyroclastic flows: Experimental design, scaling, and first results from PELE. Journal of Geophysical Research: Solid EarthVolume 120, Issue 3 p. 1487-1502. https://doi.org/10.1002/2014JB011666.

Lube, G., Cronin, S. J., Platz, T., Freundt, A., Procter, J. N., Henderson, C. & Sheridan, M. F. (2007). Flow and deposition of pyroclastic granular flows: A type example from the 1975 Ngauruhoe eruption, New Zealand. Journal of Volcanology and Geothermal Research, 161(3), 165-186.

Mason, B.G., Pyle, D.M. & Oppenheimer, C. 2004. The size and frequency of the largest explosive eruptions on Earth. Bull. Volcanol. 66, 735–748. doi:10.1007/s00445-004-0355-9.

Neri, A., Esposti Ongaro, T., Macedonio, G. & Gidaspow, D. (2003). Multiparticle simulation of collapsing volcanic columns and pyroclastc flow. Journal of Geophysical Research Atmospheres 108(B4) DOI: 10.1029/2001JB000508.

Nield, S. E. & Woods, A. W. (2004). Effects of flow density on the dynamics of dilute pyroclastic density currents. Journal of Volcanology and Geothermal Research, 132(4), 269–281. http://doi.org/10.1016/S0377-0273(03)00314-7.

Palladino, D. M., & Giordano, G. (2019). On the mobility of pyroclastic currents in light of deposit thickness and clast size trends. Journal of Volcanology and Geothermal Research, 384, 64–74. https://doi.org/10.1016/j.jvolgeores.2019.07.014.

Palladino, D.M., 2017. Simply pyroclastic currents. Bull. Volcanol. 79, 53.

Patra, A. K., Bauer, A. C., Nichita, C. C., Pitman, E. B., Sheridan, M. F., Bursik, M., Rupp, B., Webber, A., Stinton, A. J., Namikawa, L. M. & Renschler, C. S. (2005). Parallel adaptive numerical simulation of dry avalanches over natural terrain. Journal of Volcanology and Geothermal Research, 139(1–2), 1–21. https://doi.org/10.1016/j.jvolgeores.2004.06.014.

Pensa., A., Capra, L. & Giordano, G. (2019). Ash clouds temperature estimation. Implication on dilute and concentrated PDCs coupling and topography confinement. Sci Rep 9, 5657. https://doi.org/10.1038/s41598-019-42035-x.

Pensa, A., Capra, L., Giordano, G. & Corrado, S. (2018). Emplacement temperature estimation of the 2015 dome collapse of Volcán de Colima as key proxy for flow dynamics of confined and unconfined pyroclastic density currents. Journal of Volcanology and Geothermal Research. 357.

Pensa, A., Giordano, G., Cas, R. A. F. & Porreca, M. (2015). Thermal state and implications for eruptive styles of the intra-Plinian and climactic ignimbrites of the 4.6 ka Fogo A eruption sequence, São Miguel, Azores. Bulletin of Volcanology. 77(11), 99 (2015).

Pioli, L., Bonadonna, C. & Pistolesi, M. (2019). Reliability of Total Grain-Size Distribution of Tephra Deposits. Sci Rep 9, 10006. https://doi.org/10.1038/s41598-019-46125-8.

Roche, O. (2015) Nature and velocity of pyroclastic density currents inferred from models of entrainment of substrate lithic clasts. Earth and Planetary Science Letters, 418. 115-125 doi:10.1016/j.epsl.2015.03.001

Roche, O. (2012). Depositional processes and gas pore pressure in pyroclastic flows: an experimental perspective. Bull. Volcanol. 74, 1807–1820.

Roche, O., Azzaoui, N. & Guillin, A. (2021). Discharge rate of explosive volcanic eruption controls runout distance of pyroclastic density currents. Earth and Planetary Science Letters, Elsevier, 2021, 568, pp.117017. ⟨doi: 10.1016/j.epsl.2021.117017⟩.

Roche, O., Buesch, D. & Valentine, G. (2016) Slow-moving and far-travelled dense pyroclastic flows during the Peach Spring

super-eruption. Nat Commun 7, 10890. https://doi.org/10.1038/ncomms10890.
Roche, O., Philips, J. & Karim, K. (2013) Pyroclastic Density Currents. In Fagents, S., Gregg, T. K. & Lopes, R. M. (eds.) Modeling Volcanic Processes (The Physics and Mathematics of Volcanism), chap. 10, 203–229 (Cambridge University Press, Cambridge England).
Roche, O., Attali, M., Mangeney, A. & Lucas, A. (2011) On the run-out distance of geophysical gravitational flows: insight from fluidized granular collapse experiments. Earth Planet Sci Lett 311(3–4):375–385. https://doi.org/10.1016/j.epsl.2011.09.023.
Roche, O., Druitt, T. & Merle, O. (2000). Experimental study of caldera formation. Journal of Geophysical Research. 105. 395-416. 10.1029/1999JB900298.
Rosa, C. (1987). Caratteristiche geologiche e deposizionali della II colata piroclastica del Tuscolano-Artemisio ("Pozzolane Rosse" e "Pozzolane Nere" p.p. Auctorum) nel complesso vulcanico dei Colli Albani, Roma. Ph.D. Thesis.
Savage, S. B. & Hutter, K.(1989), The motion of a finite mass of granular material down a rough incline, J. Fluid Mech., 199, 177 – 215, doi:10.1017/S0022112089000340.
Scharff, L., Hort, M. & Varley, N. R. (2019). First in-situ observation of a moving natural pyroclastic density current using Doppler radar. Scientific Reports, 1–9. http://doi.org/10.1038/s41598-019-43620-w.
Shimizu, H. A., Koyaguchi, T. & Suzuki, Y. J. (2019). The run-out distance of large-scale pyroclastic density currents: a two-layer depth-averaged model. J. Volcanol. Geotherm. Res. 381, 168–184.
Silleni, A., Giordano, G., Isaia, R. & Ort M. H. (2020). The Magnitude of the 39.8 ka Campanian Ignimbrite Eruption, Italy: Method, Uncertainties and Errors. Front. Earth Sci., 19 October 2020 | https://doi.org/10.3389/feart.2020.543399.
Smith, G., Rowley, P., Williams, R., Giordano, G., Tloese, M., Silleni, A., Parsons, D.R. & Capon, S. (2020). A bedform phase diagram for dense granular currents. Nat Commun 11, 2873. https://doi.org/10.1038/s41467-020-16657-z
Sparks, R. S. J., Wilson, L. & Hulme, G. (1978). Theoretical Models = Rn B O = 200. Journal of Geophysical Research, 83(8), 1727–1739.
Sparks, R. S. J., & Walker, G. P. L. (1977). The significance of vitric-enriched air-fall ashes associated with crystal-enriched ignimbrites. Journal of Volcanology and Geothermal Research, 2(4), 329-341.
Sparks, R.S.J. & Wilson, L. (1976). A model for the formation of ignimbrite by gravitational column collapse. Journal of the Geological Society, 132, 441-451, https://doi.org/10.1144/gsjgs.132.4.0441.
Sulpizio, R., Dellino, P., Doronzo, D. M. & Sarocchi, D. (2014). Pyroclastic density currents: State of the art and perspectives. Journal of Volcanology and Geothermal Research, 283(April 2013), 36–65. https://doi.org/10.1016/j.jvolgeores.2014.06.014.
Sulpizio, R.,Mele, D., Dellino, P. & La Volpe, L., (2007). Deposits and physical properties of pyroclastic density currents during complex Subplinian eruptions: the AD 472 (Pollena) eruption of Somma-Vesuvius, Italy. Sedimentology 54, 607–635.
Trolese, M., Cerminara, M., Esposti Ongaro, T. & Giordano, G. (2019). The footprint of column collapse regimes on pyroclastic flow temperatures and plume heights. Nat Commun 10, 2476. https://doi.org/10.1038/s41467-019-10337-3.
Trolese, M., Giordano,G., Komorowski, J-C., Jenkins, S.F., Baxter, P.J., Cholik, N., Raditya, P. & Corrado, S. (2018). "Very rapid cooling of the energetic pyroclastic density currents associated with the 5 November 2010 Merapi eruption (Indonesia)." Journal of Volcanology and Geothermal Research 358: 1-12.
Trolese, M., Giordano, G., Cifelli, F., Winkler, A. & Mattei, M. (2017). Forced transport of thermal energy in magmatic and phreatomagmatic large volume ignimbrites: Paleomagnetic evidence from the Colli Albani volcano, Italy. Earth and Planetary Science Letters. 478. 179-191. 10.1016/j.epsl.2017.09.004.
Tuccimei, P., Giordano, G. & Tedeschi, M. (2006). CO2 release variations during the last 2000 years at the Colli Albani volcano (Roma, Italy) from speleothems studies. Earth and Planetary Science Letters, 243(3-4), 449-462.
Turner, J.S. (1986). Turbulent entrainment: the development of the entrainment assumption, and its application to geophysical flows. Journal of Fluid Mechanics (ISSN 0022-1120), vol. 173, Dec. 1986, p. 431-471. 10.1017/S0022112086001222.
Ui, T., Matsuwo, N., Sumita, M., & Fujinawa, A. (1999). Generation of block and ash flows during the 1990–1995 eruption of Unzen Volcano, Japan. Journal of Volcanology and Geothermal Research, 89(1-4), 123-137.
Valentine, G.A. & Sweeney, M.R. (2018) Compressible flow phenomena at inception of lateral density currents fed by collapsing gas-particle mixtures. J Geophys Res, SE 123:1286–1302. https://doi.org/10.1002/2017JB015129.
Vinkler, A. P., Cashman, K., Giordano, G., & Groppelli, G. (2012). Evolution of the mafic Villa Senni caldera-forming eruption at Colli Albani volcano, Italy, indicated by textural analysis of juvenile fragments. Journal of Volcanology and Geothermal Research, 235, 37-54.
Weit, A., Roche, O., Dubois, T. & Manga, M. (2018). Experimental Measurement of the Solid Particle Concentration in Geophysical Turbulent Gas-Particle Mixtures. Journal of Geophysical Research, American Geophysical Union, 123 (5), pp.3747 - 3761. ff10.1029/2018JB015530ff. ffhal-01914237f.
Weit, A., Roche, O., Dubois, T., & Manga, M. (2019). Maximum solid phase concentration in geophysical turbulent gas-particle flows: Insights from laboratory experiments. Geophysical Research Letters, 46, 6388– 6396. https://doi.org/10.1029/2019GL082658.
Wilson, C.J.N., (2001). The 26.5 ka Oruanui eruption, New Zealand: an introduction and overview. J. Volcanol. Geotherm. Res. 112, 133–174.
Wilson, C.J.N., Houghton, B.F., Kamp, P.J.J & McWilliams M.O. (1995). An exceptionally widespread ignimbrite with implications for pyroclastic flow emplacement Nature, 378 (1995), pp. 605-607.
Wilson, C.J.N., (1991). Ignimbrite morphology and the effects of erosion: a New Zealand case study. Bull. Volcanol., 53 (1991),

pp. 635-644.

Wilson, C. J. N., & Walker, G. P. L. (1982). Ignimbrite depositional facies: the anatomy of a pyroclastic flow. Journal of the Geological Society, 139(5), 581–592. https://doi.org/10.1144/gsjgs.139.5.0581.

Wohletz, K. H. (1998), Pyroclastic surges and compressible two-phase flow, in From Magma to Tephra, edited by Freundt, A. and Rosi, M. pp. 247–312, Elsevier, Amsterdam, Netherlands.

Figure 1.

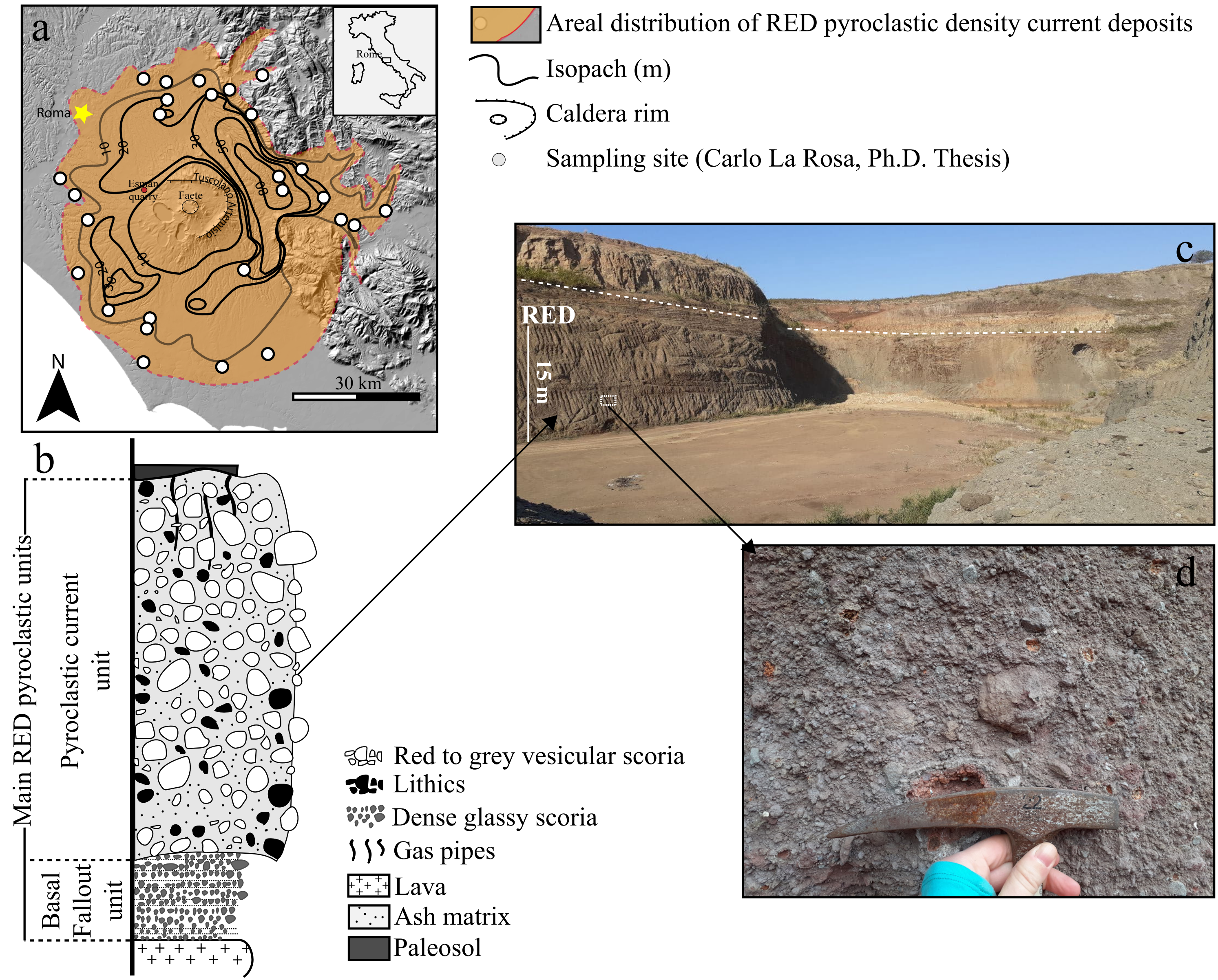

a
Roma
Rome
Esman quarry
Faete
Tuscolano Artemisio
10
20
30
50
80
70
N
30 km
Areal distribution of RED pyroclastic density current deposits
Isopach (m)
Caldera rim
Sampling site (Carlo La Rosa, Ph.D. Thesis)
b
Main RED pyroclastic units
Pyroclastic current unit
Basal Fallout unit
Red to grey vesicular scoria
Lithics
Dense glassy scoria
Gas pipes
Lava
Ash matrix
Paleosol
c
RED
15 m
d

Figure 2.

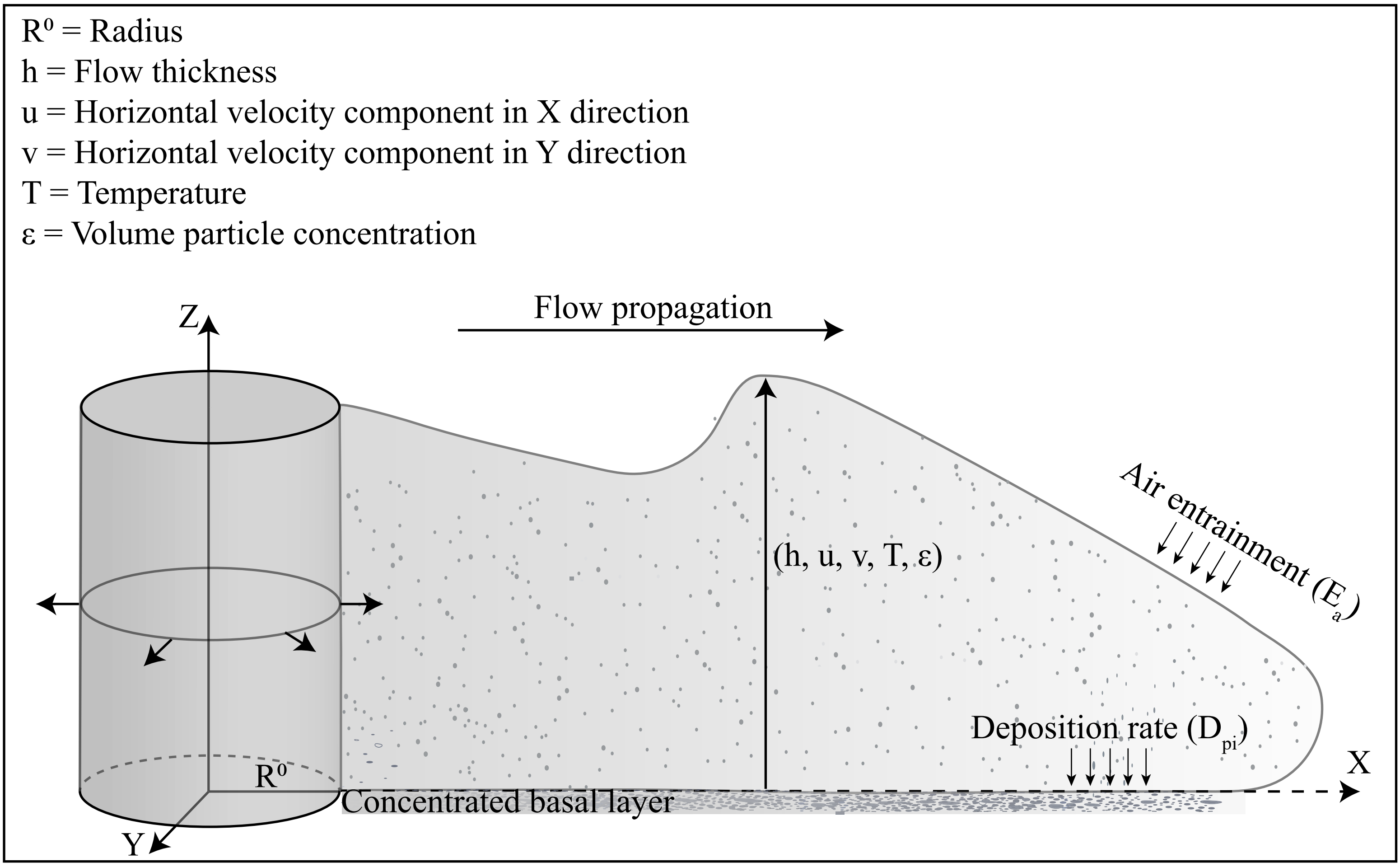

R⁰ = Radius
h = Flow thickness
u = Horizontal velocity component in X direction
v = Horizontal velocity component in Y direction
T = Temperature
ε = Volume particle concentration
Flow propagation
Z
(h, u, v, T, ε)
Air entrainment (E_a)
Deposition rate (D_pi)
X
R⁰
Concentrated basal layer
Y

Figure 3.

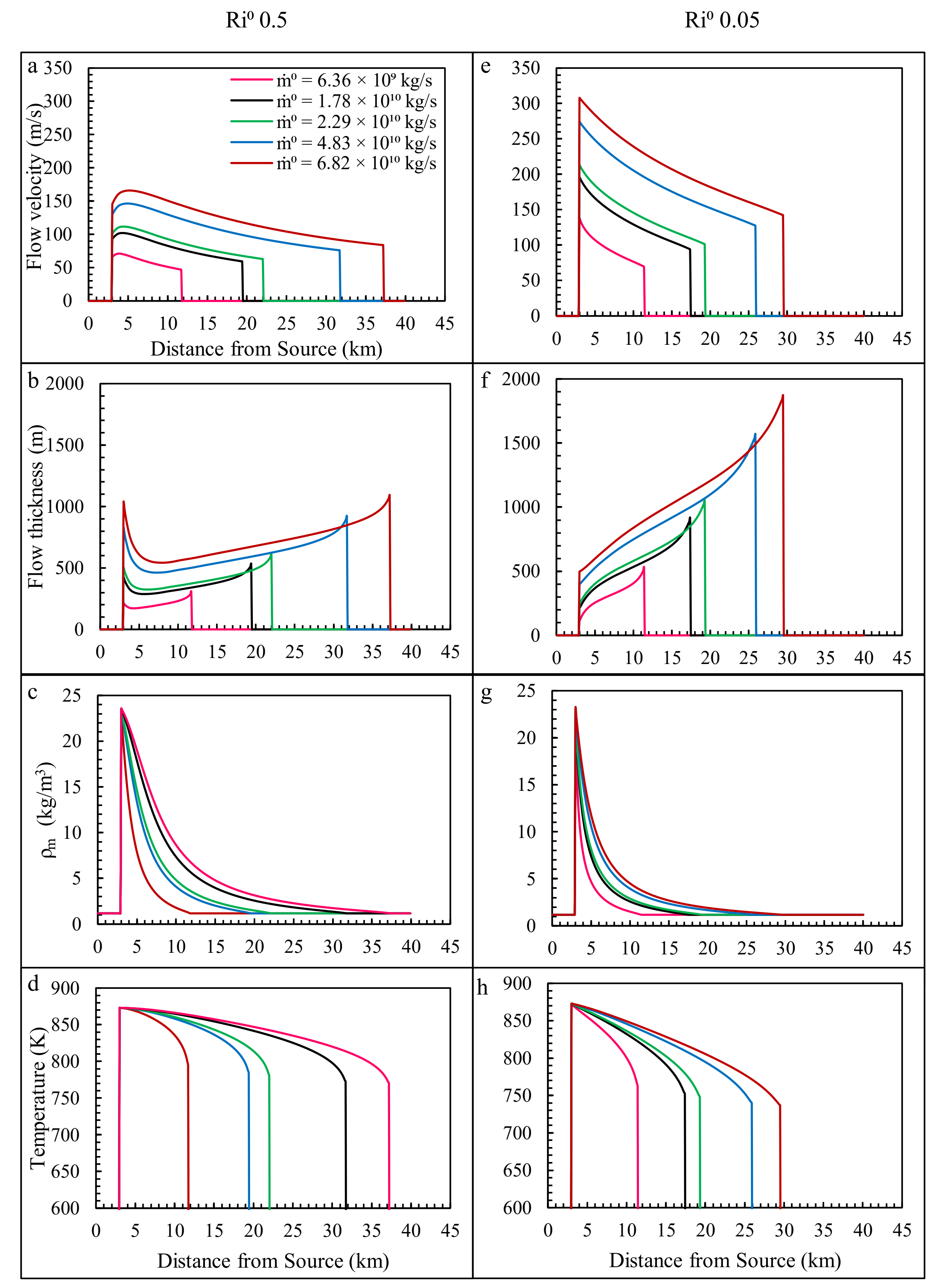

Ri⁰ 0.5
Ri⁰ 0.05
a
e
b
f
c
g
d
h
ṁ⁰ = 6.36 × 10⁹ kg/s
ṁ⁰ = 1.78 × 10¹⁰ kg/s
ṁ⁰ = 2.29 × 10¹⁰ kg/s
ṁ⁰ = 4.83 × 10¹⁰ kg/s
ṁ⁰ = 6.82 × 10¹⁰ kg/s
Flow velocity (m/s)
Flow thickness (m)
ρm (kg/m³)
Temperature (K)
Distance from Source (km)

Figure 4.

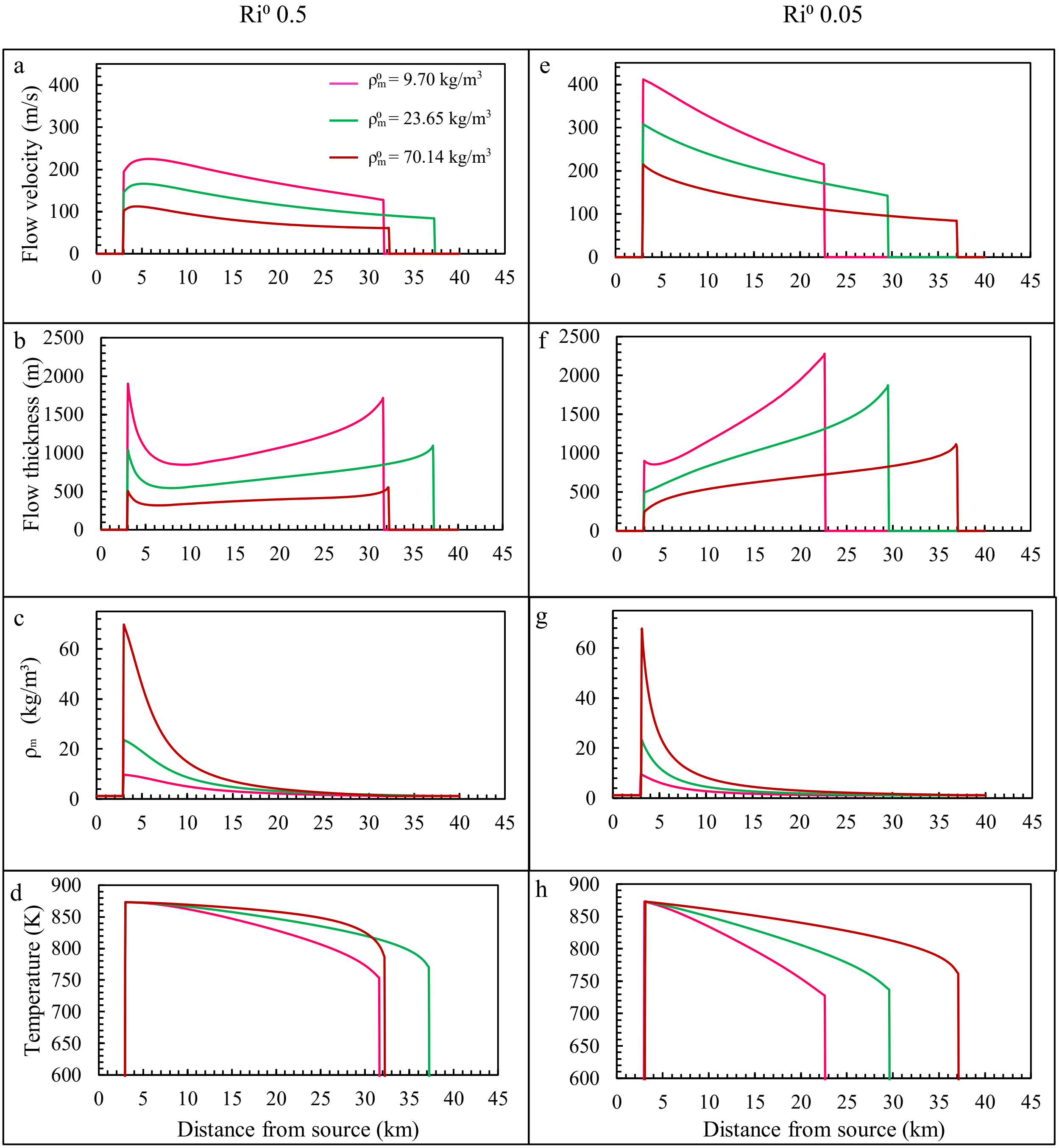

Ri⁰ 0.5
Ri⁰ 0.05
a
b
c
d
e
f
g
h
ρ_m^0 = 9.70 kg/m³
ρ_m^0 = 23.65 kg/m³
ρ_m^0 = 70.14 kg/m³
Flow velocity (m/s)
Flow thickness (m)
ρ_m (kg/m³)
Temperature (K)
Distance from source (km)
Distance from source (km)

Figure 5.

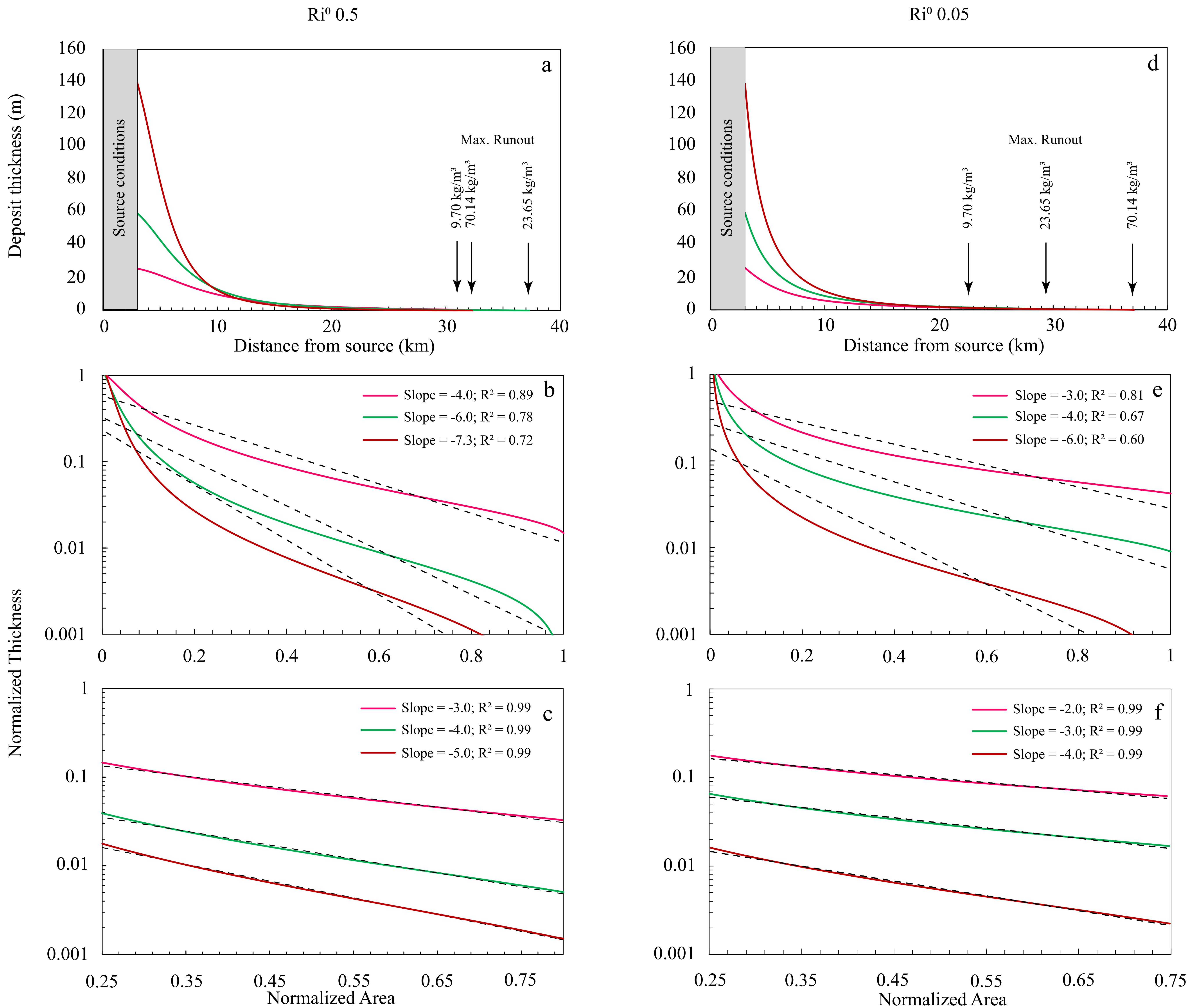

Riº 0.5
Riº 0.05
Deposit thickness (m)
Source conditions
Max. Runout
9.70 kg/m³
70.14 kg/m³
23.65 kg/m³
Distance from source (km)
a
d
Normalized Thickness
Slope = -4.0; R² = 0.89
Slope = -6.0; R² = 0.78
Slope = -7.3; R² = 0.72
b
Slope = -3.0; R² = 0.81
Slope = -4.0; R² = 0.67
Slope = -6.0; R² = 0.60
e
Slope = -3.0; R² = 0.99
Slope = -4.0; R² = 0.99
Slope = -5.0; R² = 0.99
c
Slope = -2.0; R² = 0.99
Slope = -3.0; R² = 0.99
Slope = -4.0; R² = 0.99
f
Normalized Area

Figure 6.

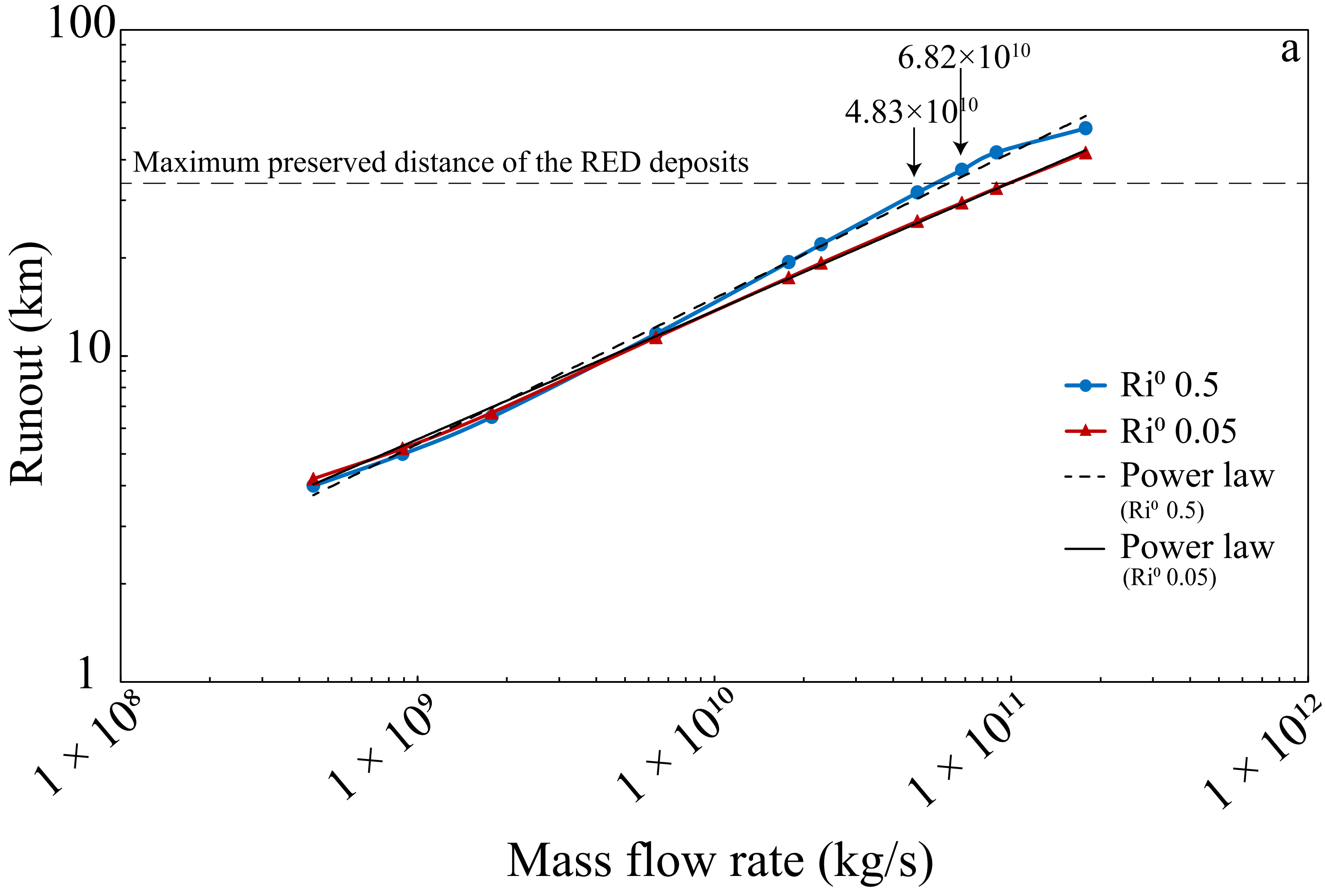

100
10
1
Runout (km)
a
6.82×10^10
4.83×10^10
Maximum preserved distance of the RED deposits
Ri⁰ 0.5
Ri⁰ 0.05
Power law
(Ri⁰ 0.5)
Power law
(Ri⁰ 0.05)
1 × 10^8
1 × 10^9
1 × 10^10
1 × 10^11
1 × 10^12
Mass flow rate (kg/s)

Figure 7.

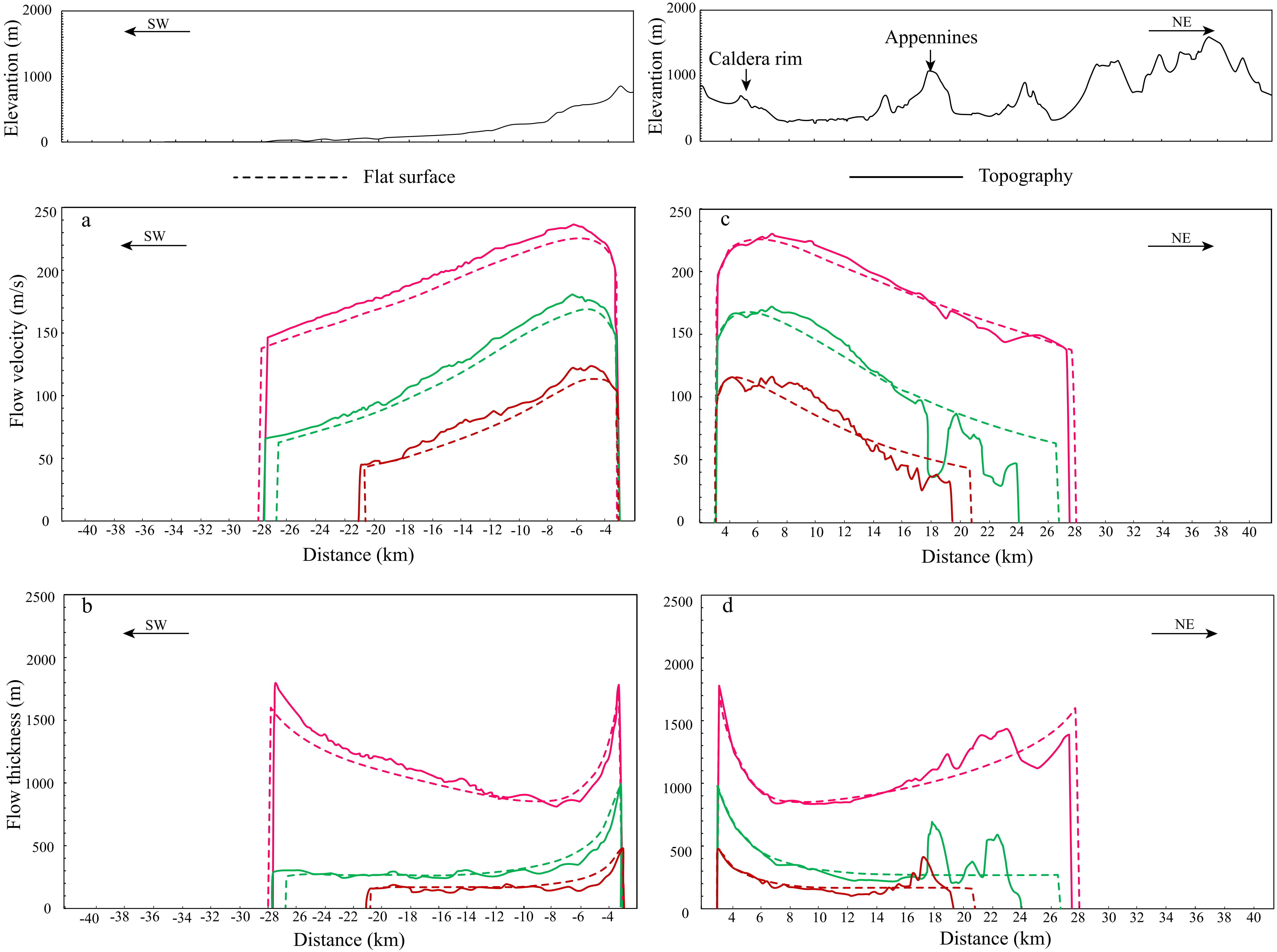

SW
NE
Elevantion (m)
Caldera rim
Appennines
Flat surface
Topography
a
b
c
d
Flow velocity (m/s)
Flow thickness (m)
Distance (km)

Figure 8.

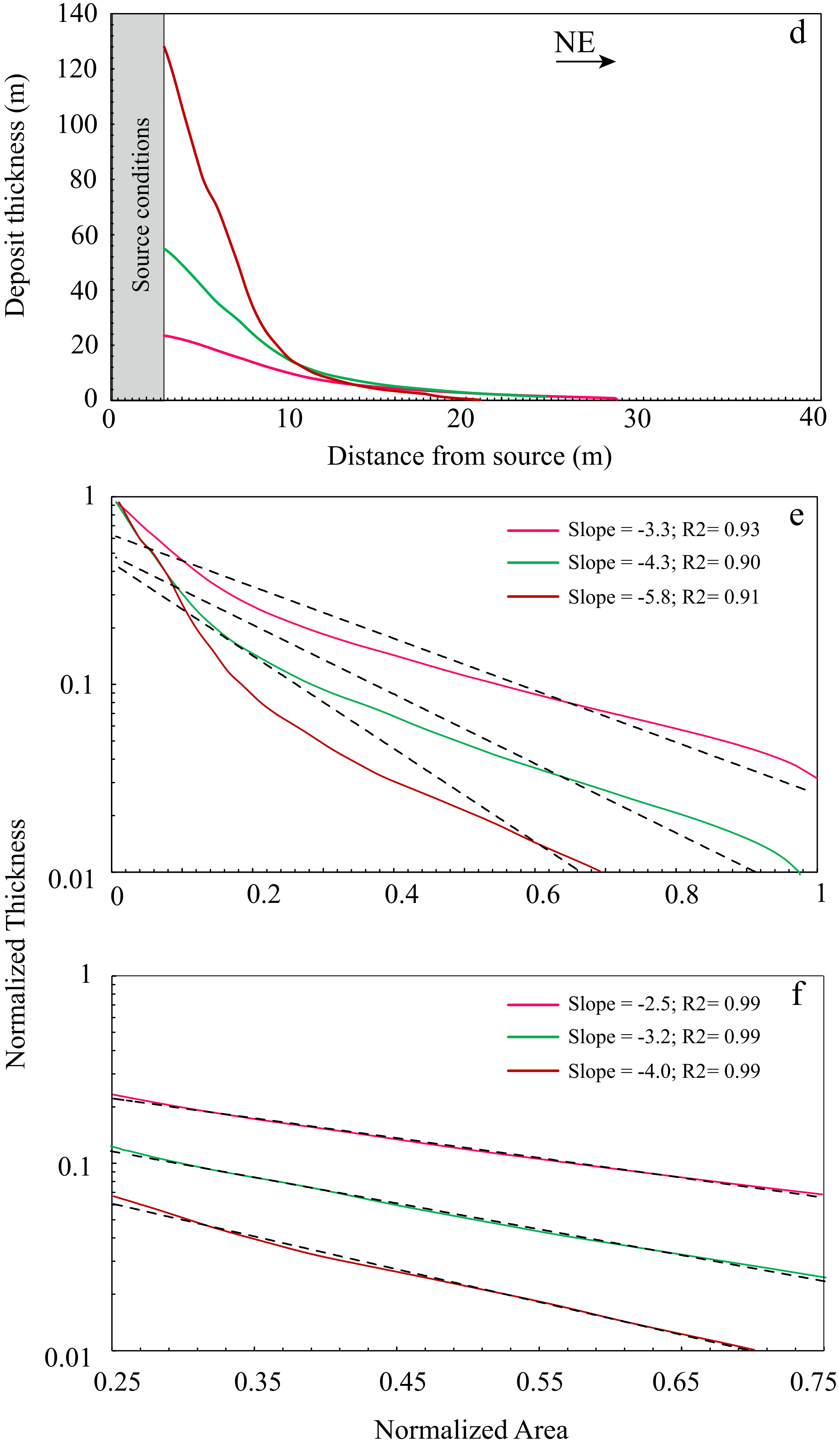

Deposit thickness (m)
Source conditions
NE
d
Distance from source (m)
e
Slope = -3.3; R2= 0.93
Slope = -4.3; R2= 0.90
Slope = -5.8; R2= 0.91
Normalized Thickness
f
Slope = -2.5; R2= 0.99
Slope = -3.2; R2= 0.99
Slope = -4.0; R2= 0.99
Normalized Area

Figure 9.

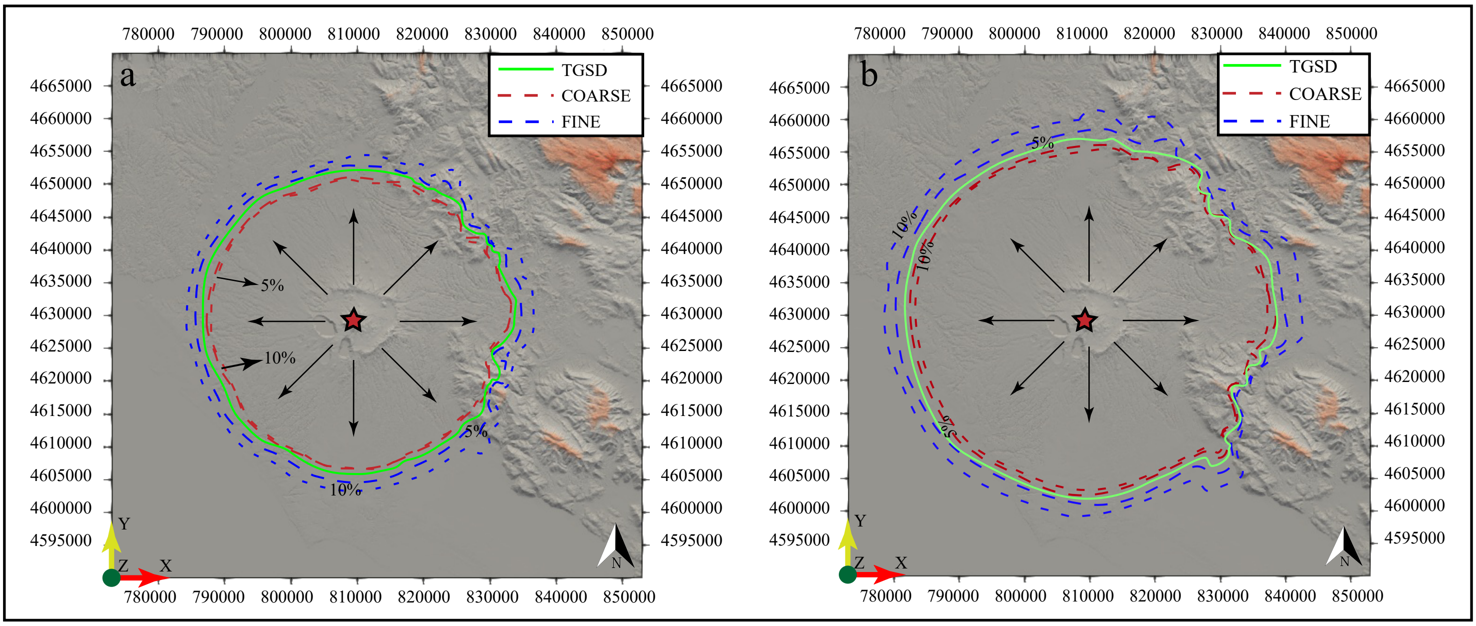
a
b
TGSD
COARSE
FINE
5%
10%
780000
790000
800000
810000
820000
830000
840000
850000
4665000
4660000
4655000
4650000
4645000
4640000
4635000
4630000
4625000
4620000
4615000
4610000
4605000
4600000
4595000
X
Y
Z
N

Figure 10.

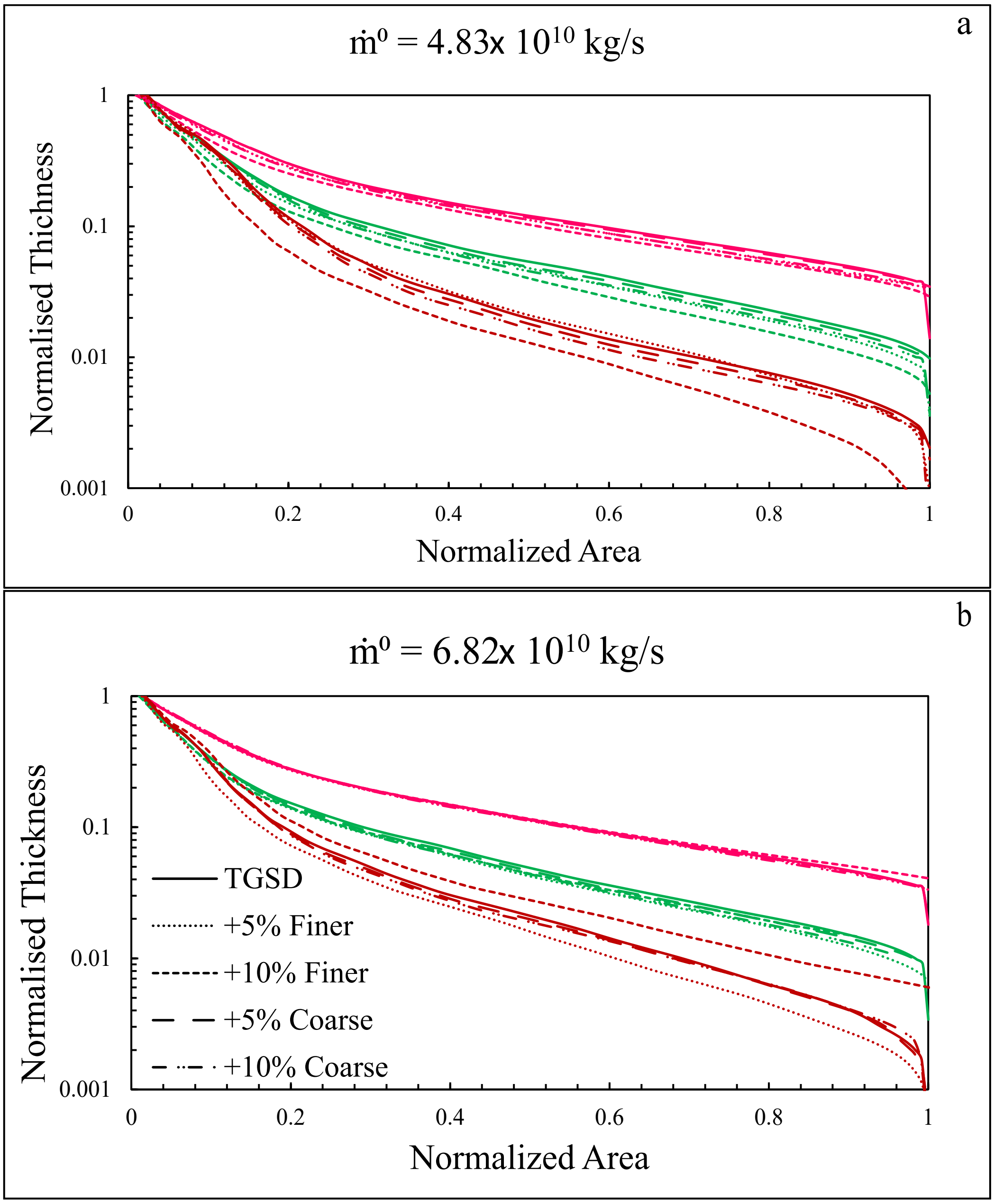
a
$\dot{m}^0 = 4.83x\ 10^{10}$ kg/s
Normalised Thichness
Normalized Area
1
0.1
0.01
0.001
0
0.2
0.4
0.6
0.8
1
b
$\dot{m}^0 = 6.82x\ 10^{10}$ kg/s
Normalised Thickness
Normalized Area
TGSD
+5% Finer
+10% Finer
+5% Coarse
+10% Coarse
1
0.1
0.01
0.001
0
0.2
0.4
0.6
0.8
1

Figure 11.

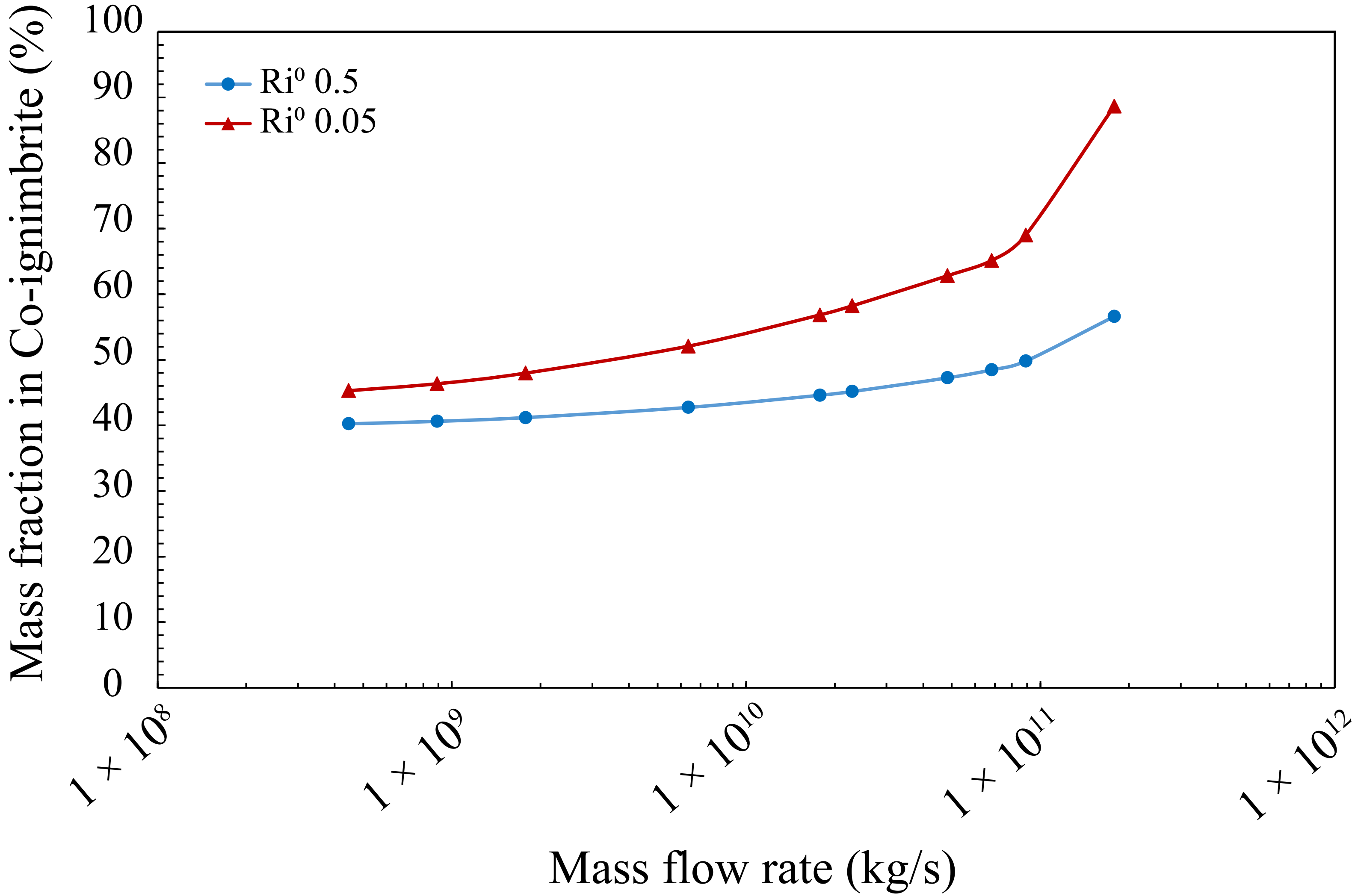

Mass fraction in Co-ignimbrite (%)
100
90
80
70
60
50
40
30
20
10
0
Ri⁰ 0.5
Ri⁰ 0.05
1 × 10^8
1 × 10^9
1 × 10^10
1 × 10^11
1 × 10^12
Mass flow rate (kg/s)

Figure 12.

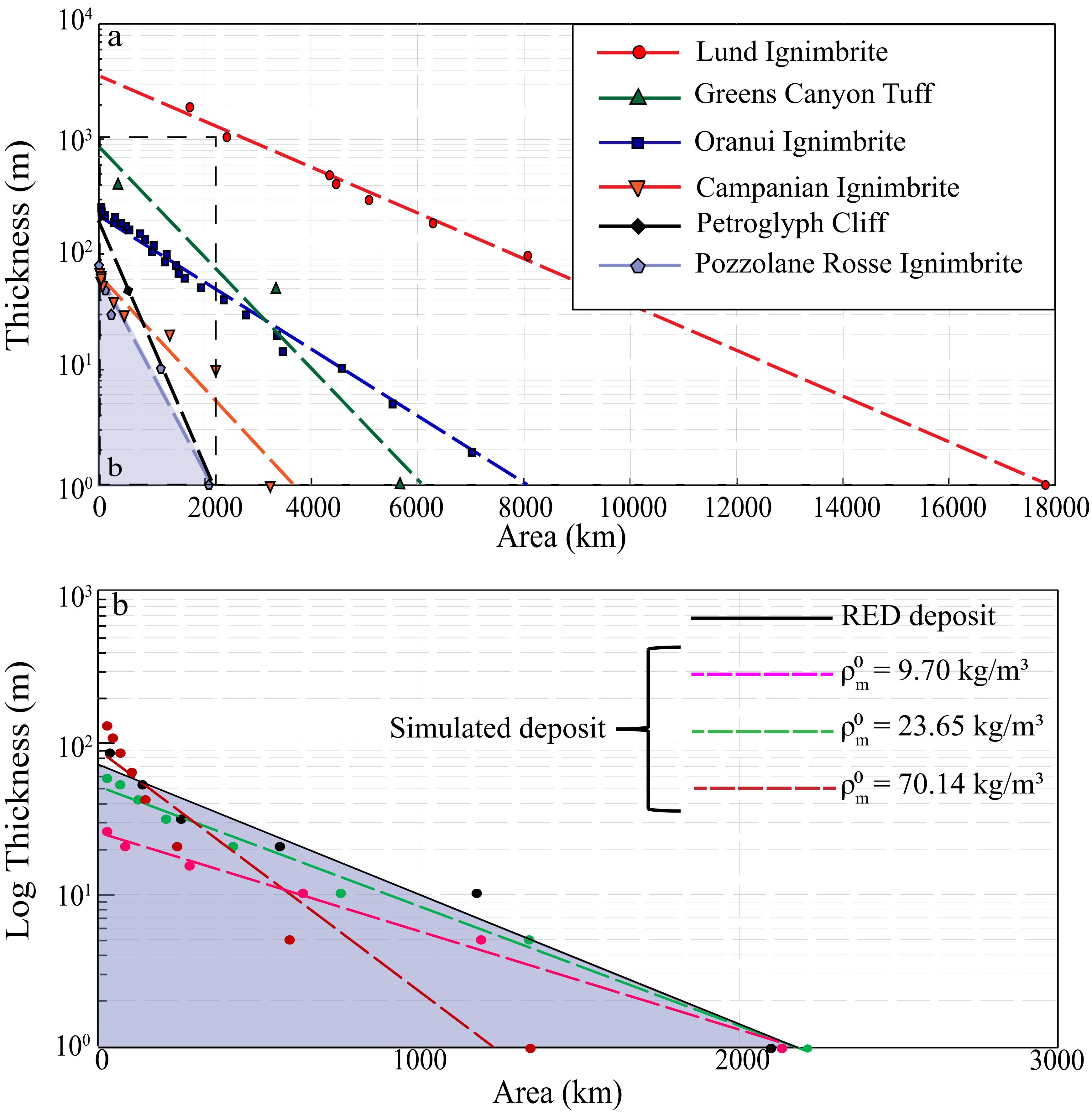

a
Lund Ignimbrite
Greens Canyon Tuff
Oranui Ignimbrite
Campanian Ignimbrite
Petroglyph Cliff
Pozzolane Rosse Ignimbrite
Thickness (m)
Area (km)
b
RED deposit
Simulated deposit
ρ0m = 9.70 kg/m³
ρ0m = 23.65 kg/m³
ρ0m = 70.14 kg/m³
Log Thickness (m)
Area (km)

Table 1: Input parameters used in the simulations, resulting from an interval of $\dot{m}^0$ between 10^9 and 10^{10} kg/s. $\dot{m}^0$: initial mass flow rate; r^0: initial radius; T^0: initial temperature; ε^0: initial volume particle fraction; h^0: initial flow thickness; v^0: initial flow velocity; ρ_m^0: initial mixture density; Ri^0: initial Richardson number.1: 200 µm; 2: 1 mm; 3: 1.6 cm.

	ID	$\dot{m}^0$ *(kg/s)*	T^0 *(K)*	$\varepsilon^0_{1,2,3}$	ρ^0_m *(kg/m³)*	h^0 *(m)*	v^0 *(m/s)*
Ri 0.5	*Run1*	6.36×10^9	873-973	0.005	23.65	219.39	65.01
	Run2	1.78×10^{10}	873-973	0.005	23.65	435.84	91.67
	Run3	2.29×10^{10}	873-973	0.005	23.65	515.27	99.69
	Run4	4.83×10^{10}	873-973	0.005	23.65	848.07	127.89
	Run5	6.82×10^{10}	873-973	0.005	23.65	1066.88	143.43
Ri 0.05	*Run6*	6.36×10^9	873-973	0.005	23.65	101.84	140.14
	Run7	1.78×10^{10}	873-973	0.005	23.65	202.3	197.52
	Run8	2.29×10^{10}	873-973	0.005	23.65	239.19	214.78
	Run9	4.83×10^{10}	873-973	0.005	23.65	393.64	275.52
	Run10	6.82×10^{10}	873-973	0.005	23.65	495.2	309.01

Table 2: Input parameters used in the simulations, resulting from an initial density ρ_m^0 of 9.70 kg/m^3, 23.65 kg/m^3 and 70.14 kg/m^3. $\dot{m}^0$ initial mass flow rate; r^0: initial radius; T^0: initial temperature; ε^0: initial volume particle fraction; h^0: initial flow thickness; v^0: initial flow velocity; ρ_m^0: initial mixture density; Ri^0: initial Richardson number. *1: 200 μm; 2: 1 mm; 3: 1.6 cm.*

	ID	$\dot{m}^0$ *(kg/s)*	T^0 *(K)*	$\varepsilon^0_{1,2,3}$	ρ_m^0 *(kg/m³)*	h^0 *(m)*	v^0 *(m/s)*
Ri 0.5	*Run11*	6.82×10^{10}	873-973	0.015	70.14	514.9	100.21
	Run12	6.82×10^{10}	873-973	0.005	23.65	1066.88	143.43
	Run13	6.82×10^{10}	873-973	0.002	9.70	1947.37	191.5
Ri 0.05	*Run16*	6.82×10^{10}	873-973	0.015	70.14	238.99	215.91
	Run17	6.82×10^{10}	873-973	0.005	23.65	495.2	309.01
	Run18	6.82×10^{10}	873-973	0.002	9.70	903.89	412.58

Table *3*: Values in percentage of the mass fractionation in the deposit (% M_{dep}) and in the Coignimbrite (% M_{co}). $\dot{m}^0$ is the initial mass flow rate; Ri^0 is the initial Richardson number. % $M_{200\mu m}$ is mass percentage deposits for 200 µm particles. % M_{1mm} is mass percentage deposits for 1mm. %$M_{1.6cm}$ is mass percentage deposits for 1.6 cm particles.

	ID	$\dot{m}0$ (kg/s)	% M_{dep}	% $M_{200\mu m}$	% M_{1mm}	% $M_{1.6cm}$	% M_{co}	% $M_{200\mu m}$	% M_{1mm}	% $M_{1.6cm}$
Ri 0.5	*Run1*	6.36×10^{9}	57.25	34.35	62.87	81.33	42.75	65.65	37.13	18.67
	Run2	1.78×10^{10}	55.40	30.68	62.14	81.34	44.6	53.52	37.86	18.66
	Run3	2.29×10^{10}	54.68	29.64	61.83	81.33	45.32	70.2	37.81	18.67
	Run4	4.83×10^{10}	52.75	26.03	60.33	81.32	47.25	40.95	39.67	18.68
	Run5	6.82×10^{10}	51.16	24.16	59.2	81.28	48.47	75.84	40.8	18.72
Ri 0.05	*Run6*	6.36×10^{9}	47.92	19.35	54.93	80.99	52.08	80.65	45.07	19.01
	Run7	1.78×10^{10}	43.16	14.62	48.04	79.56	56.84	85.38	51.96	20.44
	Run8	2.29×10^{10}	41.78	13.51	45.94	78.82	58.22	86.49	54.06	21.18
	Run9	4.83×10^{10}	37.19	10.45	39.08	75.16	62.81	89.55	60.92	24.84
	Run10	6.82×10^{10}	34.86	9.18	35.74	72.61	65.14	90.82	64.26	27.39

Table 4: Input parameters for sensitivity analysis to volume fraction effect.

	Mass fraction		
	200 μm	1 mm	1.6 cm
TGSD	0.12	0.77	0.11
+5% Finer	0.17	0.73	0.1
+10% Finer	0.22	0.68	0.09
+5% Coarse	0.11	0.73	0.16
+10% Coarse	0.1	0.69	0.2